AGU ADVANCING EARTH AND SPACE SCIENCE

Tectonics

RESEARCH ARTICLE

10.1029/2020TC006314

Key Points:

- Thermochronological data quantifying the tectonic history of the undocumented northern edge of the Peruvian Altiplano (Abancay Deflection)
- 3D thermokinematic models unravel the evolution of the Eastern Cordillera and the Altiplano
- Steady and uniform exhumation between 40 and 5 Ma, followed by tectonically driven tilting of the Eastern Cordillera

Supporting Information:

Supporting Information may be found in the online version of this article.

Correspondence to:

B. Gérard,
benjamin.gerard.alpes@gmail.com

Citation:

Gérard, B., Robert, X., Audin, L., Valla, P. G., Bernet, M., & Gautheron, C. (2021). Differential exhumation of the Eastern Cordillera in the Central Andes: Evidence for south-verging backthrusting (Abancay Deflection, Peru). *Tectonics*, *40*, e2020TC006314. https://doi.org/10.1029/2020TC006314

Received 27 MAY 2020
Accepted 25 FEB 2021

Differential Exhumation of the Eastern Cordillera in the Central Andes: Evidence for South-Verging Backthrusting (Abancay Deflection, Peru)

Benjamin Gérard[1,4], Xavier Robert[1], Laurence Audin[1], Pierre G. Valla[1,2], Matthias Bernet[1], and Cécile Gautheron[3]

[1]Université Grenoble Alpes, IRD, ISTerre, CNRS, Grenoble, France, [2]Institut of Geological Sciences, University of Bern, Bern, Switzerland, [3]Université Paris-Saclay, CNRS, GEOPS, Orsay, France, [4]Now at GET, Université de Toulouse, CNRS, IRD, UPS, Toulouse, France

Abstract Located at the northern tip of the Altiplano, the Abancay Deflection marks abruptly the latitudinal segmentation of the Central Andes spreading over the Altiplano to the south and the Eastern Cordillera northward. The striking morphological contrast between the low-relief Altiplano and the high-relief Eastern Cordillera makes this area a well-suited place to determine spatiotemporal variations in surface and/or rock uplift and discuss the latest phase of the formation of the Central Andes. Here, we aim to quantify exhumation and uplift patterns in the Abancay Deflection since 40 Ma and present new apatite (U–Th)/He and fission track data from four altitudinal profiles and additional individual samples. Age–elevation relationships and thermal modeling both document that the Abancay Deflection experienced a moderate, spatially uniform, and steady exhumation at 0.2 ± 0.1 km/Myr between 40 and ∼5 Ma implying common large-scale exhumation mechanism(s). From ∼5 Ma, while the northern part of the Eastern Cordillera and the Altiplano registered similar ongoing slow exhumation, the southern part of the Eastern Cordillera experienced one order-of-magnitude of exhumation acceleration (1.2 ± 0.4 km/Myr). This differential exhumation since ∼5 Ma implies active tectonics, river capture, and incision affecting the southern Eastern Cordillera. 3D thermokinematic modeling favors a tectonic decoupling between the Altiplano and the Eastern Cordillera through backthrusting activity of the Apurimac fault. We speculate that the Abancay Deflection, with its "bulls-eye" structure and significant exhumation rate since 5 Ma, may represent an Andean protosyntaxis, similar to the syntaxes described in the Himalaya or Alaska.

1. Introduction

The Central Andes contain the second-highest and widest plateau on Earth: The Altiplano. This wide morphologic domain spreading over 350–400 km of maximum width is characterized by low relief sustained by an overthickened crust of ∼60 km (Allmendinger et al., 1997; James, 1971). Andean topography building started during the Cretaceous (∼120–110 Ma; Jaillard & Soler, 1996). Tectonic, climatic, and erosional interactions affecting the Altiplano and its eastward border, the Eastern Cordillera (Figure 1), have been extensively studied in the southern Central Andes (Bolivia, Argentina; Strecker et al., 2007). The northern edge of the Altiplano, namely the Abancay Deflection (southern Peru; Dalmayrac et al., 1980; B. Gérard et al., 2021; Marocco, 1971), however, has been poorly documented, although its relief and structural organization reveals uncommon features with curved faults, deflected drainage basins and rivers, and deeply incised landforms. The Abancay Deflection occupies a part of the Altiplano to the south and the Eastern Cordillera northward (Figures 1 and 2) and is limited to the north by the Subandes. Morphologically, the Altiplano and the Eastern Cordillera acquired their respective modern mean elevation of ∼4 and ∼4.5 km before 5 Ma (Sundell et al., 2019). Although having experienced similar timing and magnitude of surface uplift, the Altiplano and the Eastern Cordillera are quite different in terms of morphology and geology. In comparison, the Eastern Cordillera presents prominent landscape relief enhanced by deep incision and much older bedrock lithologies (Paleozoic for the Eastern Cordillera vs. Meso-Cenozoic for the Altiplano; Figure 2a). The Subandes represent the most recent domain in terms of orogen building and corresponds to the eastward propagation of Andean deformation through successive fold and thrust fronts since the

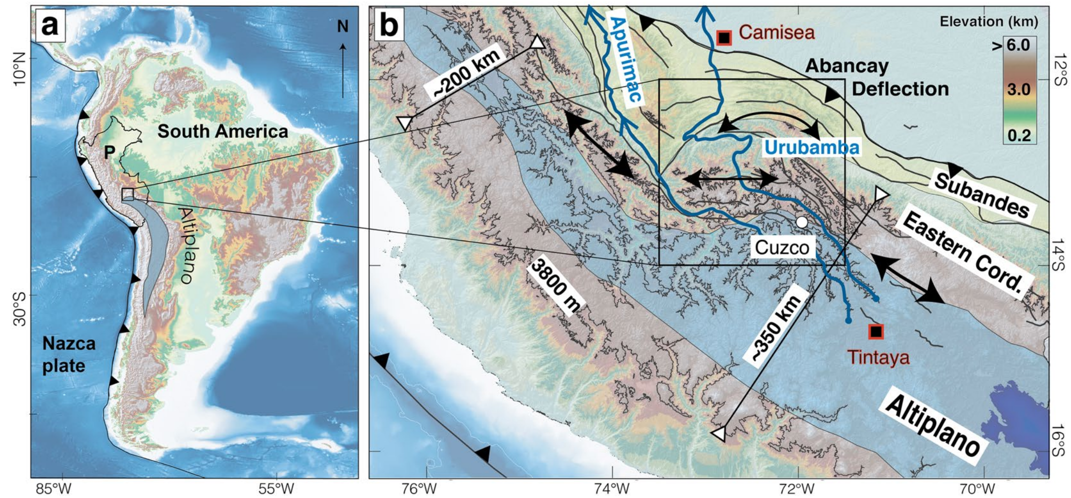

Figure 1. Abancay Deflection location. (a) Location within South America of the study area at the northern tip of the Altiplano in Peru (P). (b) Zoom-in on the Abancay Deflection area (black square in (a)). Double black arrows highlight the topography elongation axis. Note the pronounced incision within the study area through the isoelevation line (black) at 3.8 km elevation via the Urubamba and Apurimac rivers (blue) canyons. Black thin lines framed by white triangles highlight the latitudinal range width variation with the Abancay Deflection as the transition zone between the northern narrow Peruvian Andes and the southern wide Bolivian Orocline. Black squares with red borders are the places where thermal parameters were measured.

Miocene (Espurt et al., 2011), tectonically involving Paleozoic and Cenozoic deposits in thin and thick-skinned mode (Figure 2a; Gautheron et al., 2013).

Mechanisms for exhumation of the Bolivian and southern Peruvian Eastern Cordillera are debated and imply either east-verging thrusting along a ramp connected to the Subandean zone (Gotberg et al., 2010; Rak et al., 2017) or reactivation of inherited faults as west-verging backthrusts (Perez, Horton, & Carlotto, 2016), both with subsequent erosion of the built topography. All these geometries and kinematics are nonetheless not mutually exclusive. In Bolivia, the Eastern Cordillera experienced exhumation between 50 and 15 Ma with transfer of tectonic deformation to the Subandean zone at ca. 15 Ma (Barnes et al., 2012). From thermochronological records, the northern Altiplano has been suggested to have experienced a steady exhumation of ~0.2 km/Myr between around 40 and 15 Ma (Ruiz et al., 2009). However, the limited records before 38 Ma and after 14 Ma for this area prevent deciphering and/or speculating between different exhumation dynamics and drivers. Quantification of the exhumation history could give insights regarding surface uplift under specific geological conditions (England & Molnar, 1990), the lack of exhumation data does not allow to discuss surface-uplift scenarios such as slow and continuous surface uplift associated with (lower) crustal deformation since 40 Ma (Barnes & Ehlers, 2009; Husson & Sempere, 2003; Ouimet & Cook, 2010), versus potential surface-uplift acceleration during the Miocene triggered by lithospheric delamination event(s) (Garzione et al., 2017). The high-relief Eastern Cordillera seems to register a more recent and complex exhumation history (<5 Ma) with both topographic incision and regressive erosion (B. Gérard et al., 2021; Lease & Ehlers, 2013). Regarding the climatic imprint on the Eastern Cordillera, major canyon carving is supposedly related to Pliocene global climate cooling (Lease & Ehlers, 2013). Nonetheless, increased orographic precipitation in such a rising orogen (Insel et al., 2010) could explain also canyon incision events earlier than the Pliocene (Poulsen et al., 2010).

Although the timing of surface uplift and mechanisms of exhumation are debated, a clear contrast and decoupling in terms of vertical motion between the Altiplano, the Eastern Cordillera, and the Subandes has emerged (Garzione et al., 2017). Our aim is to provide further quantitative constraints to unravel the mechanisms triggering the Abancay Deflection exhumation since 40 Ma and discuss exhumation rates and timing in relation to large-scale surface-uplift information. The deeply incised Abancay Deflection is the ideal target to unravel the long-term evolution of the northern edge of the Altiplano (Figure 1). Here, we present new apatite (U–Th)/He (AHe) and fission track (AFT) data, targeting Permo-Triassic (Mišković et al., 2009)

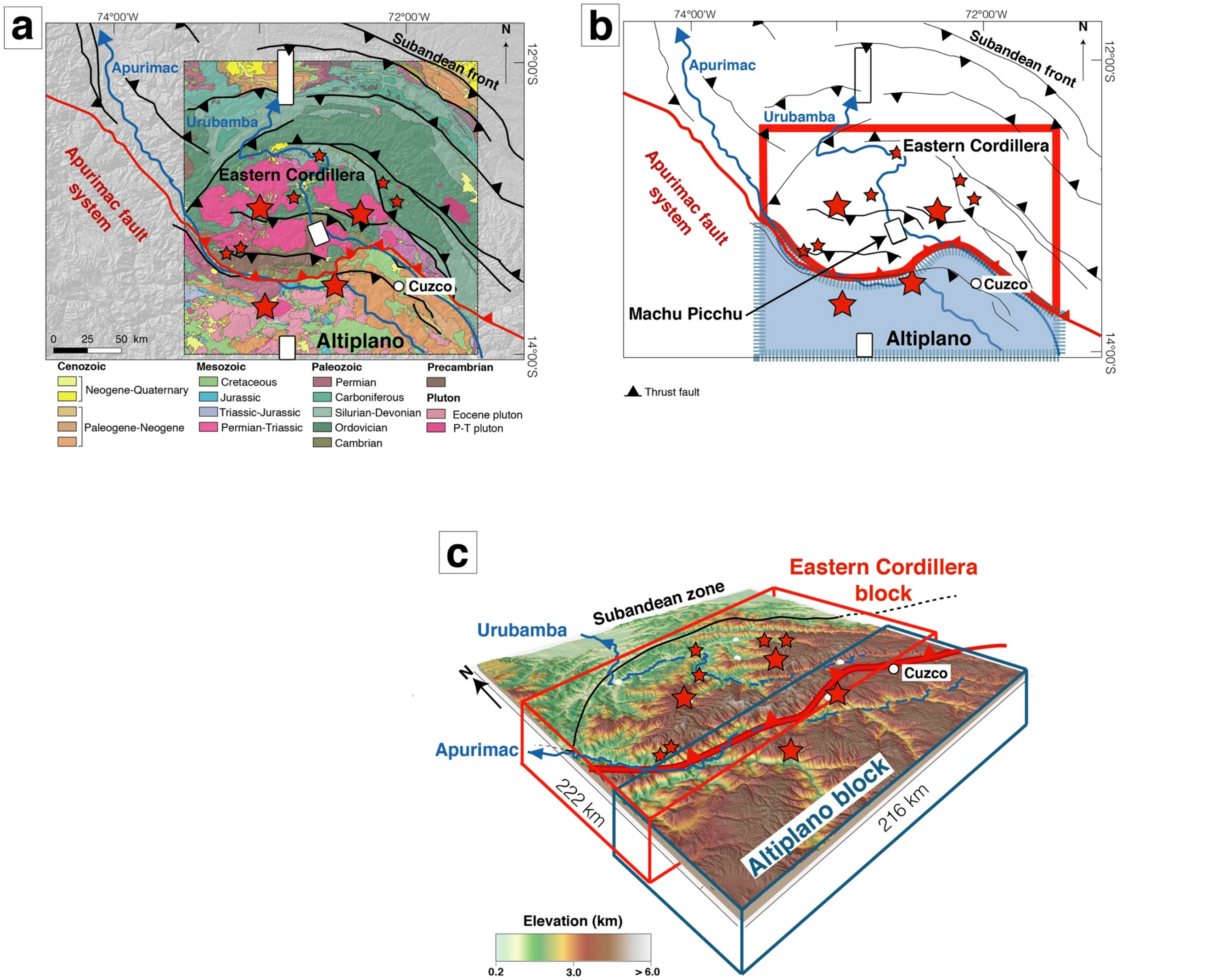

Figure 2. Geology and morphology of the Abancay Deflection. (a) Geological map of the study area. The crustal-scale Apurimac fault system marks the tectonic limit between the Altiplano and the Eastern Cordillera. (INGEMMET geological map database—1:100,000). White rectangles refer to previous thermochronological studies; references are provided in Sections 3 and 4. (b) Simplified map (from (a)) with major lithotectonic domains: the Altiplano in blue and the Eastern Cordillera framed in red. (c) 3D DEM of the Abancay Deflection. On panels, red stars are the thermochronological sample location (vertical profiles and individual data; this study). 2D colored area (b) and corresponding 3D views (c) are crustal-block locations processed with 3D thermokinematics modeling using Pecube for the Altiplano (blue) and the Eastern Cordillera (red) blocks.

and Paleogene (Carlier et al., 1996; Mamani et al., 2010) plutonic bedrock along high-relief valleys. We interpret the thermochronological data using age–elevation relationships (AERs; Glotzbach et al., 2011), thermal (2D; QTQt; Gallagher, 2012) and thermokinematic (3D; Pecube; Braun, 2003; Braun et al., 2012) modeling to determine the late Eocene to modern exhumation history of the Abancay Deflection and discuss potential exhumation mechanisms.

2. Geological Setting

The Abancay Deflection connects the Central and Northern Andes in Peru; its hinge-like character is emphasized by the >45° deflection of its fault pattern from the overall NNW-SSE axis of the range (Figure 2a; Marocco, 1971). This region is directly located above the slab dip transition of the Nazca oceanic plate (Figure 1) from "flat" (northward) to "normal" (southward) subduction (Barazangi & Isacks, 1976). The study area encompasses the distinct morphotectonic regions of the Altiplano to the south and the

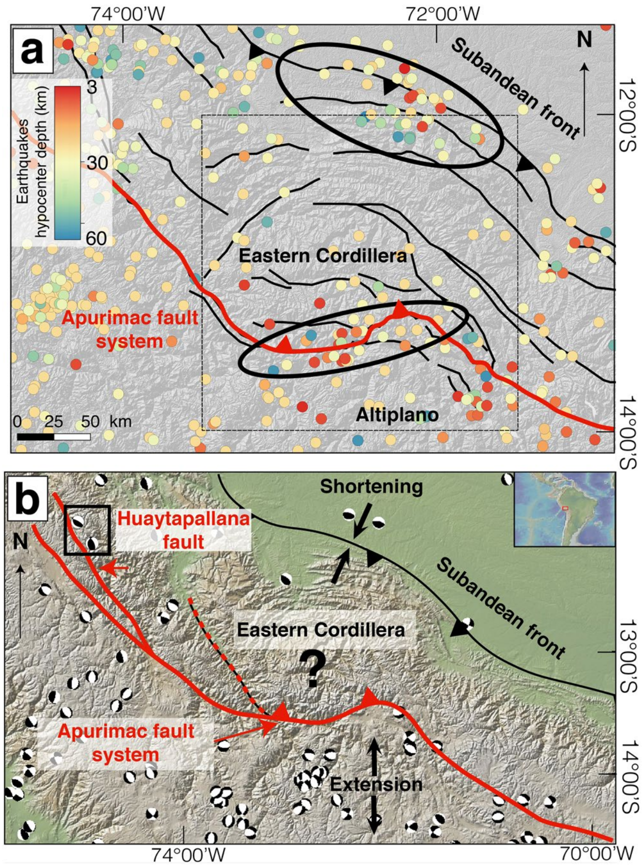

Figure 3. Crustal seismic map of the Abancay Deflection (dashed squares; hypocenters < 60 km; Mw > 2). (a) Mapped earthquakes come from the USGS, IGP and ISC databases. Regions included into black ellipses emphasize positive anomalous cluster of seismicity in comparison with the quiescent Abancay core of the Eastern Cordillera. Black lines represent the major thrusts of the studied area. (b) Moment tensors (CMT) for earthquakes (1969–2019) for the Abancay Deflection region (Dziewonski et al., 1981; Ekström et al., 2012). Focal mechanisms (transpressional) for the two 1969 Huaytapallana events are framed by the black rectangle (Dorbath et al., 1990; Suárez et al., 1983). There are no CMT data for Mw < 5.5 earthquakes. Tectonic shortening characterizes the Subandean front, whereas extensional mechanisms affect the Altiplano. The question mark refers to the unknown tectonic behavior for the Eastern Cordillera.

Eastern Cordillera to the north, separated by the regional crustal-scale Apurimac fault system (Figure 2; Carlier et al., 2005). This fault system marks the northern limit of the Arequipa terrane accreted to South America at 1 Ga (Loewy et al., 2004; Ramos, 2008). In the Eastern Cordillera, the existing relationships between lithospheric thinning and magmatism suggest that the Apurimac fault system seems to affect the study area since at least the Late Permian (by a strike-slip fault in an extensional context; Sempere et al., 2002) which remarkably shows the long-term tectonic inheritance of the region. Eocene–early Oligocene plutons (50–30 Ma; Mamani et al., 2010) emplaced into Meso-Cenozoic sedimentary rocks (Carlier et al., 1996) crop out in the high-elevation and low-relief Altiplano. This domain was exhumed steadily at moderate rates (~0.2 km/Myr), at least between 38 and 14 Ma (Ruiz et al., 2009). In contrast, Permo-Triassic batholiths are dominant in the higher and deeply incised Eastern Cordillera and intruded into lower Paleozoic rocks (Figure 2; Mišković et al., 2009). Preliminary thermochronological data (AFT ages of ~2 Ma; Kennan, 2008) of two samples, from the core of the Abancay region, suggest rapid and recent exhumation for the Eastern Cordillera. Thermal perturbation linked to magmatic arc activity ceased after ca. 30 Ma and the latest local and sporadic volcanic events (from 7 to 0.5 Ma; Bonhomme et al., 1988; Carlier et al., 1996) focused along the Apurimac fault system mostly south east of Cuzco (Bonhomme et al., 1988). Inherited deflected faults and arched-captured rivers characterize the Abancay Deflection on the northern edge of the Altiplano. The Abancay Deflection records high-magnitude counterclockwise tectonic rotation of up to 65° during the late Eocene–early Miocene (~40–20 Ma; Butler et al., 1995; Richards et al., 2004; Roperch et al., 2006, 2011) and possibly more recently (since ~12 Ma; Rousse et al., 2005) in a Bolivian Orocline bending context (Müller et al., 2002). In such context, according to the single study available with microstructural analysis (Dalmayrac et al., 1980), it appears that the Abancay Deflection mainly recorded left-lateral tectonic deformation since the late Eocene, possibly associated with a limited vertical component. This sinistral shear behavior is also supported by paleomagnetic data obtained close to Cuzco (Gilder et al., 2003). In addition, it appears that the Eastern Cordillera did not experience any burial during the Eocene, since it acted like a long-lived structural high as suggested by the lack of a Meso-Cenozoic sedimentary cover (except for Quaternary fluvial and landslide deposits of limited spatial extent; Figure 2a; Perez, Horton, & Carlotto, 2016; Perez, Horton, Mcquarrie, et al., 2016). Finally, at least since the early Cenozoic, the Eastern Cordillera was high enough to prevent sediment transfer from the Western Cordillera to the Amazonian basin and was also an eroding area, representing a sediment source toward both the Altiplano to the southwest and the Amazonian basin to the northeast (Perez, Horton, & Carlotto, 2016; Perez, Horton, Mcquarrie, et al., 2016).

The Subandean zone and the Altiplano are documented as tectonically active; with shortening since ~14 Ma in the Subandes (Espurt et al., 2011; Gautheron et al., 2013; Figure 3) and extension since ~5 Ma in the Altiplano (Cabrera et al., 1991; Figure 3). In between, the Eastern Cordillera, limited southward by the Apurimac fault system presents nowadays a low-magnitude crustal seismicity, which mainly focuses along the Altiplano–Eastern Cordillera limit (Figure 3a). It is, however, too low to determine any specific tectonic behavior (Figure 3b). Preliminary thermochronological investigation in the core of the Eastern Cordillera (Machu Picchu; Figure 2b), nonetheless, favors a post ~4 Ma acceleration of incision-driven exhumation with the capture of a northern-extended paleo-Altiplano along with potential tectonic activity of the Apurimac fault system (B. Gérard et al., 2021). However, this inference has been restricted to the

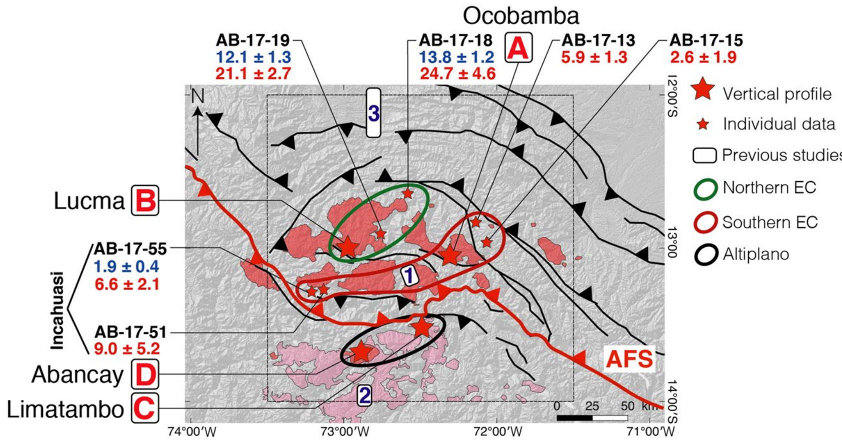

Figure 4. Sample locations of the new thermochronological ages within the Abancay Deflection. Red and pink polygons are, respectively, Permo-Triassic and Eocene plutons. Previous studies are (1) B. Gérard et al. (2021), and Kennan (2008); (2) Ruiz et al. (2009); (3) Espurt et al. (2011) and Gautheron et al. (2013). Blue and red numbers below sample names refer to AHe mean ages and AFT central ages for individual samples and the two-sampled-point Incahuasi vertical profile. Red capital letters refer to the other sampled vertical profiles (A, Ocobamba profile; B, Lucma profile; C, Limatambo profile; D, Abancay profile). Profiles results are displayed in Figure 6. Green, red, and black contours mark the latitudinal segmentation of the Abancay Deflection defining three areas according to thermal histories modeled with QTQt (i.e., Northern EC, Southern EC, and Altiplano, respectively). The black dashed square frames the Abancay Deflection. AHe, apatite (U–Th)/He; AFT, apatite fission track; EC, Eastern Cordillera.

area of Machu Picchu and cannot be extended yet for the entire Abancay Deflection. Also, this preliminary study can neither validate nor invalidate potential tectonic-driven exhumation. The observed seismicity for the Apurimac fault system area could be linked and/or connected with either Subandean flat-ramp thrust systems or undocumented active internal backthrusts, or even normal faulting as currently occurring in the Altiplano (Wimpenny et al., 2020). Potential tectonic drivers responsible for building the Abancay Deflection and particularly the Eastern Cordillera area remain unknown. Quantitative thermochronology and modeling are ideal tools that enable us to explore exhumation patterns over the whole area and to discuss the possible exhumation mechanisms.

3. Methods

AHe and AFT thermochronology are based on He and fission track production during alpha decay of ^{238}U, ^{235}U, ^{232}Th, and ^{147}Sm and fission decay of ^{238}U, respectively, with associated ^{4}He and fission track accumulation within apatite crystals. Using a rate of He diffusion out of the crystals or fission track annealing with temperature, those methods can be used to record the thermal evolution of the upper crust, given their thermal sensitivity ranges spanning from ~80°C to 40°C (Ault et al., 2019) and ~75°C to 125°C (Reiners & Brandon, 2006), respectively, for active mountain ranges, depending on cooling rate and/or holding time within the respective partial retention or annealing zones. Thus, low-temperature thermochronology records the thermal evolution of the upper crust (<5 km) and is a key to decipher between different exhumation mechanisms through time-evolving rock uplift and landscape evolution (Ault et al., 2019; Reiners & Shuster, 2009). Quantitative interpretation with three different types of models (i.e., geometric, thermal, and thermokinematic, Sections 3.2–3.4) with increasing complexity makes it possible to test model robustness and propose consistent scenarios for the exhumation of the Abancay Deflection.

3.1. Low-Temperature Thermochronological Data

We collected 33 samples from igneous bedrock along four altitude profiles (Ocobamba, Lucma, Abancay, and Limatambo) complemented by six individual samples across the Abancay Deflection, in order to get an optimal coverage of the study area (Figures 2 and 4; Table 1). Granite samples were crushed and sieved at the Géode Laboratory (Lyon, France) to extract the 100–160-μm grain size fractions. Apatite crystals were

Table 1
Sample Locations and Bedrock Lithologies

Sample number	Latitude (°S)	Longitude (°W)	Elevation (m)	Lithology	Geologic unit	Pluton period	Pluton age (Ma)	Reference
Ocobamba profile[a]								
AB-17-05	13.091198	72.26337	3,903	Granite	Mesapelada pluton	Permian	277 ± 2	Reitsma (2012)
AB-17-06	13.07867	72.27952	3,696	Granite	Mesapelada pluton	Permian	277 ± 2	Reitsma (2012)
AB-17-07	13.07128	72.2803	3,447	Granite	Mesapelada pluton	Permian	277 ± 2	Reitsma (2012)
AB-17-08	13.05875	72.28962	3,190	Granite	Mesapelada pluton	Permian	277 ± 2	Reitsma (2012)
AB-17-11	13.00978	72.3299	2,450	Monzonite	Mesapelada pluton	Permian	277 ± 2	Reitsma (2012)
Individual data								
AB-17-13	12.83221	72.14085	1,638	Granite	Colca pluton	Carboniferous	330 ± 10	Lancelot et al. (1978)
AB-17-15	12.9652	72.07252	2,475	Granite	Colca pluton	Carboniferous	330 ± 10	Lancelot et al. (1978)
AB-17-18	12.64752	72.55498	912	Granite	Quellotuno pluton	Permian	282 ± 1	Reitsma (2012)
AB-17-19	12.89585	72.74471	1,362	Granite	Kiteni pluton	Permian	279 ± 2	Reitsma (2012)
Lucma profile[a]								
AB-17-21	13.04408	72.88454	2,235	Granite	Kiteni pluton	Permian	257 ± 3	Lancelot et al. (1978)
AB-17-22	13.04171	72.93961	3,020	Granite	Kiteni pluton	Permian	257 ± 3	Lancelot et al. (1978)
AB-17-23	13.02889	72.9593	3,678	Granite	Kiteni pluton	Permian	257 ± 3	Lancelot et al. (1978)
AB-17-25	13.00124	72.9468	4,050	Granite	Kiteni pluton	Permian	257 ± 3	Lancelot et al. (1978)
AB-17-26	13.03244	72.9577	3,589	Granite	Kiteni pluton	Permian	257 ± 3	Lancelot et al. (1978)
AB-17-28	13.05984	72.9371	2,609	Granite	Kiteni pluton	Permian	257 ± 3	Lancelot et al. (1978)
Limatambo profile[a]								
AB-17-29	13.5299	72.43471	4,056	Diorite	Cotabamba pluton	Paleogene	40 ± 2	Perello et al. (2003)
AB-17-30	13.53367	72.45849	3,795	Diorite	Cotabamba pluton	Paleogene	40 ± 2	Perello et al. (2003)
AB-17-31	13.5419	72.4688	3,581	Diorite	Cotabamba pluton	Paleogene	40 ± 2	Perello et al. (2003)
AB-17-32	13.52771	72.4671	3,322	Diorite	Cotabamba pluton	Paleogene	40 ± 2	Perello et al. (2003)
AB-17-33	13.51888	72.47569	2,966	Diorite	Cotabamba pluton	Paleogene	40 ± 2	Perello et al. (2003)
AB-17-34	13.50543	72.4702	2,740	Diorite	Cotabamba pluton	Paleogene	40 ± 2	Perello et al. (2003)
AB-17-35	13.50373	72.47325	2,586	Diorite	Cotabamba pluton	Paleogene	40 ± 2	Perello et al. (2003)
AB-17-36	13.49839	72.48075	2,435	Diorite	Cotabamba pluton	Paleogene	40 ± 2	Perello et al. (2003)
Abancay profile[a]								
AB-17-37	13.67147	72.89801	2,800	Monzonite	Abancay orthogneiss	Triassic	222 ± 7	Lancelot et al. (1978)
AB-17-38	13.67129	72.90512	2,573	Diorite	Abancay orthogneiss	Triassic	222 ± 7	Lancelot et al. (1978)
AB-17-39	13.6721	72.90939	2,280	Gabbro	Abancay orthogneiss	Triassic	222 ± 7	Lancelot et al. (1978)
AB-17-40	13.68018	72.91482	1,916	Granite	Abancay orthogneiss	Triassic	222 ± 7	Lancelot et al. (1978)
AB-17-41	13.68651	72.84196	4,136	Granite	Abancay orthogneiss	Triassic	222 ± 7	Lancelot et al. (1978)
AB-17-42	13.67414	72.85007	3,753	Granite	Abancay orthogneiss	Triassic	222 ± 7	Lancelot et al. (1978)
AB-17-43	13.66636	72.86651	3,459	Granitic arena	Abancay orthogneiss	Triassic	222 ± 7	Lancelot et al. (1978)
AB-17-44	13.6792	72.88035	3,209	Granitic arena	Abancay orthogneiss	Triassic	222 ± 7	Lancelot et al. (1978)
Incahuasi profile[a]								
AB-17-51	13.2918	73.15121	3,434	Granite	Chucuito pluton	Ordovician	475 ± 5	Reitsma (2012)
AB-17-55	13.30613	73.21085	2,455	Granite	Chucuito pluton	Ordovician	475 ± 5	Reitsma (2012)

Note. The geologic unit and pluton period columns refer to the studies of Egeler and De Booy (1961), Lancelot et al. (1978), Mišković et al. (2009), Perello et al. (2003), and Reitsma (2012) and the INGEMMET geological database.
[a]Profile names were given considering the main cities nearby the investigated area.

concentrated using standard magnetic and heavy-liquid separation techniques at the GeoThermoChronology (GTC) platform within the ISTerre laboratory (Université Grenoble Alpes, France).

For AHe dating, single euhedral apatite crystals were carefully selected under a binocular microscope to identify minerals without fractures and/or inclusions that would skew the AHe age (diffusion artifacts and/or additional ^{4}He sources; Farley, 2002). We determined the individual grain geometry and calculated the alpha-ejection correction factor using the Qt_FT program (Gautheron & Tassan-Got, 2010; Ketcham et al., 2011). Individual apatites were encapsulated in platinum tubes allowing apatite heating and manipulation. Each apatite in its platinum tube was then heated under high vacuum conditions at high temperature (1,050°C ± 50°C using an infrared diode laser) twice for 5 min at GEOPS laboratory (Université Paris-Saclay, France). The released ^{4}He gas was mixed with a known amount of ^{3}He, purified, and the gas was analyzed using a Prisma Quadrupole. The ^{4}He content was determined by isotope dilution method. Subsequently, apatite crystals were dissolved in 100 μL of HNO_3 5 N solution containing known amount of ^{235}U, ^{230}Th, ^{149}Sm, and ^{42}Ca. The solution was heated at 70°C during 3 h and after a cooling time, 900 μL of distilled water was added. The final solution was analyzed using an ELEMENT XR ICP-MS and the ^{238}U, ^{230}Th, and ^{147}Sm concentrations and apatite weight (using the Ca content) were determined following the methodology proposed by Evans et al. (2005). Durango apatite crystals were also analyzed during the same period to ensure the data quality. The one-sigma error on each AHe age amounts to 8%, reflecting the analytical error and the uncertainty on the F_T ejection factor correction. More details about the analytical procedure can be found in Recanati et al. (2017).

For AFT dating at the GTC laboratory (ISTerre, Grenoble, France), apatites were mounted in epoxy resin, polished, and etched for 20 s at 21°C using a 5.5 M HNO_3 solution to reveal spontaneous fission tracks. Using the external detector method, all samples were irradiated together with Durango and Fish Canyon Tuff age standards and IRMM540R dosimeter glasses at the FRM II reactor (Munich, Germany). Tracks were counted and horizontally confined track lengths were measured dry at 1,250X magnification under an Olympus BX51 optical microscope, using the FTStage 4.04 program at ISTerre. We used the BINOMFIT program (Ehlers et al., 2005) to calculate the AFT central ages (Figures S1–S27).

3.2. Age–Elevation Relationships

For AER modeling, single-tier or multitier age–elevation relationships to the AFT and AHe data from an altitudinal profile data were fitted using a Bayesian approach to obtain a first-order estimate of apparent exhumation rates and to possibly evidence any potential break-in-slope in AERs by minimization of the Bayesian Information Criterion (BIC; Glotzbach et al., 2011; Schwarz, 1978). The BIC provides a statistical way to assess the appropriate model complexity (Schwarz, 1978) by computing the ratio between likelihood (fitting) and the model complexity (number of break-in-slope; Glotzbach et al., 2011). This statistical approach implies that the lower the BIC value is for different scenarios (i.e., one single or multiple segment(s) for a given AER), statistically the more robust is the inferred slope of the AER in terms of apparent exhumation rate. In our study, we only present and interpret the outcome scenarios that minimize the BIC criterion. This approach provides first-order constraints on the exhumation rates and potential exhumation changes through time for each altitudinal profile. These apparent exhumation rates are, nonetheless, not incorporating any consideration regarding the intersample AHe/AFT kinetic variability, the thermal crustal regime, the relief evolution, and the isostasy assuming a quasi-vertical profile (Stüwe et al., 1994). These modeling biases will be considered with 2D thermal and 3D thermokinematic modeling described hereafter.

3.3. Time–Temperature Modeling (QTQt)

Time–temperature modeling with QTQt (Bayesian transdimensional and Markov chain Monte Carlo sampling; Gallagher, 2012) gives quantitative constraints regarding thermal histories for individual samples, with the possibility to combine multisamples from pseudo vertical profiles. We processed 300,000 iterations for both individual sample and profiles exploring predicted *T*–*t* paths with their respective likelihood to extract best fitting thermal histories (Figures S28–S37). We used the implemented annealing model of Ketcham et al. (2007) and the radiation damage model of Gautheron et al. (2009) for AFT and AHe data, respectively. We allowed the geothermal gradient to vary over time between 10 and 40°C/km which are common for the nonvolcanic Central Andes (Barnes et al., 2008). The total timespan explored considers 2 times the older thermochronological age for each profile to eliminate any potential temporal bias.

Assessing the geothermal gradient is a crucial point for exhumation rate computation, and the Abancay Deflection is devoid of any direct measurement. We computed a geothermal gradient according to the nearest thermal parameter measurements and/or accepted values. Using heat flow and thermal conductivity measurements at the Tintaya mine 100 km south-east of Cuzco in the Altiplano (40 mW/m^2 and 2.9 W/m/°C, respectively; Figure 1b; Henry & Pollack, 1988), crustal average heat production (~0.9 μW/m^3; Springer, 1999), thermal diffusivity for granitic bedrock (~40 km^2/Myr; Arndt et al., 1997; Whittington et al., 2009), and a 25°C surface temperature (Gonfiantini et al., 2001), we obtained a geothermal gradient of 18 ± 4°C/km (Text S1). This computed value is consistent with direct measurements inferred from the Camisea area (~17°C/km; Figure 1b; Espurt et al., 2011) and the Tintaya mine (~14°C/km; Henry & Pollack, 1988). Moreover, this value overlaps with compiled geothermal gradients for the Eastern Cordillera in Bolivia (26 ± 8°C/km; Barnes et al., 2008).

Following QTQt modeling, we thus convert cooling histories derived from QTQt expected models into exhumation rates, using an assumed constant and spatially uniform geothermal gradient of 18 ± 4°C/km. We report the 95% confidence interval around the expected models. This method leads to averaging and smoothing of the predicted cooling histories but is a conservative approach. With these estimates, in addition to the AER and Pecube outcomes, we can compare exhumation rates between these different and independent approaches to identify consistency in model predictions or any potential impact of different assumptions in the modeling approaches. Magmatic arc activity at the Abancay Deflection and its potential thermal perturbation ceased after ~30 Ma (Mamani et al., 2010). It appears that the Eastern Cordillera did not experience any burial during the Eocene, because it acted like a long-lived structural high (Perez, Horton, & Carlotto, 2016; Perez, Horton, Mcquarrie, et al., 2016), as mentioned earlier. Furthermore, Cenozoic basins only occurred in the Altiplano domain (Figure 2a), which prevented potential sedimentary burial in our study area. For the Altiplano, most of the sedimentary cover was deposited synchronously with the magmatic arc activity prior to 30 Ma (Figure 2a; Mamani et al., 2010) and even prior to ~40 Ma considering the crystallization age of the Cotabamba pluton we sampled (Limatambo profile; Table 1; Perello et al., 2003). We consequently assumed that all samples in the Altiplano were at temperatures higher than the closure temperature before the onset of cooling in our QTQt models (interpreted from 40 Ma). For the surface, we implemented an atmospheric lapse rate of 6°C/km according to Gonfiantini et al. (2001) for the eastern flank of the intertropical Andes. Parameters used for QTQt data inversion are displayed in Table S1.

3.4. Thermokinematic Modeling (Pecube)

3.4.1. Pecube Model

Pecube modeling allows to quantify thermal histories for rock particles at depth in exhumation or burial contexts, considering landscape evolution (topography, relief), the thermal regime of the crust, the tectonic setting (faults, uplift or subsidence), and isostasy (Braun, 2003; Braun et al., 2012). Pecube modeling offers the possibility to simultaneously test numerous tectonic or incision scenarios in 3D, computing associated thermal histories, and to subsequently compare numerical predictions to observed thermochronological data (punctual or along altitudinal profiles). By solving the 3D heat equation in the crust, the thermokinematic program Pecube v4.2 (Braun, 2003; Braun et al., 2012) predicts the spatial distribution of thermochronological ages for specific samples considering exhumation through lateral and vertical rock kinetics and relief evolution. We used Pecube in inverse mode (Neighborhood Algorithm [NA]; Sambridge, 1999a, 1999b) to determine optimal value ranges for tested parameters by minimizing the misfit function between predictions and observations (Text S2).

3.4.2. Input Data and Fixed Parameters

We implemented into Pecube thermochronological data including AFT and AHe thermochronometric systems. We used 33 AHe ages (AHe mean grain ages, 28 new data and 5 from B. Gérard et al. [2021]) and 42 AFT ages (AFT central ages, 32 new data, 2 from Kennan [2008], and 8 from Ruiz et al. [2009]). We implemented the present-day topography extracted from the global elevation database GTOPO30 (Figure 5). The He diffusion coefficient and the AFT annealing model from Farley (2000) and Ketcham et al. (1999) have

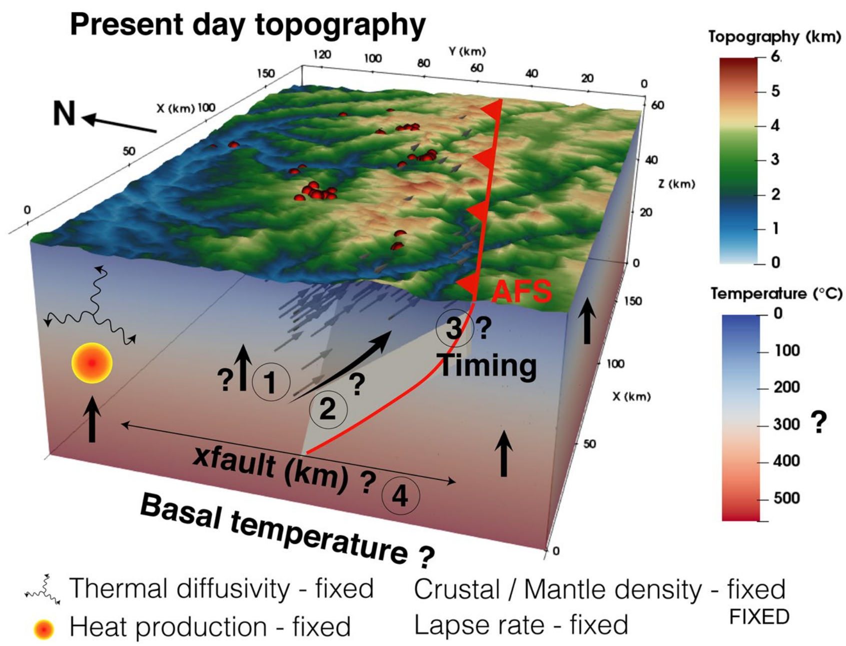

Figure 5. Parameters implemented and/or explored in Pecube through time. Example for the Eastern Cordillera crustal block (see Figure 2 for location). For the Altiplano block, we only explored the crustal-block exhumation (1). Red dots mark the location of the thermochronological data. Numbers and question marks refer to explored parameters. (1) Crustal-block exhumation (km/Ma); (2) fault velocity (km/Ma); (3) timing of fault activation (Ma); (4) x fault (km), proxy for the fault geometry (fault dip). AFS, Apurimac fault system. Additional details are given in Table S4 and Figure S38.

been used, respectively. For AHe data, we chose the Farley (2000) model for He diffusion as it presents mean values for the diffusion coefficient for low-damaged apatites. In our case, as exhumation histories are simple without identified reheating, damage influence may play a minor role in the He diffusion process and is nearly identical to the Gautheron et al. (2009) diffusion model in such a case. It is not possible with Pecube to reproduce the AHe age dispersion between crystals due to damage impact on He diffusion (Gautheron et al., 2009; Shuster et al., 2006). So, we here decided to implement the AHe mean ages and standard deviation errors (Table S2). Regarding the AFT data, we also implemented track-length measurements when available. Finally, we also subsequently compared the Pecube model *T*–*t* outcomes (best fitting scenarios) to *T*–*t* paths derived from QTQt modeling.

In order to optimize computation time, we divided the Abancay Deflection into two crustal blocks (Altiplano and Eastern Cordillera; Figure 2) that we modeled independently. Each of these crustal blocks represents the natural tectonomorphic boundary of the Abancay Deflection. The timespan explored starts at 50 Ma for all the simulations to eliminate any potential temporal bias. We subsequently divided the explored timespan into six time slices: 50, 25, 15, 10, 5, and 0 Ma. For each time boundary, we fit the modeled mean paleoelevation according to Sundell et al. (2019). We do not have, however, any information regarding the relief evolution of the Abancay Deflection, which sits in a remote location with no existing information about relief evolution (Text S4). Finally, for exhumation rate quantification from thermochronological data, we fixed the crustal thermal and rheological parameters in space and time (Figure 5 and Table S3). For these parameters, we finally explored the basal temperature of the crustal block and the thermal diffusivity to test our chosen geothermal gradient (Table S4).

3.4.3. Neighborhood Algorithm Inversions and Explored Parameters

We used Pecube in inverse mode to quantitatively constrain parameter values (i.e., tectonomorphic scenarios) that best reproduce the input thermochronological data. We extracted the best fitting parameter values for each inversion computing probability density functions (Sambridge, 1999a, 1999b). When the inversion clearly converges toward a unique parameter solution (one peak for the probability density function), we

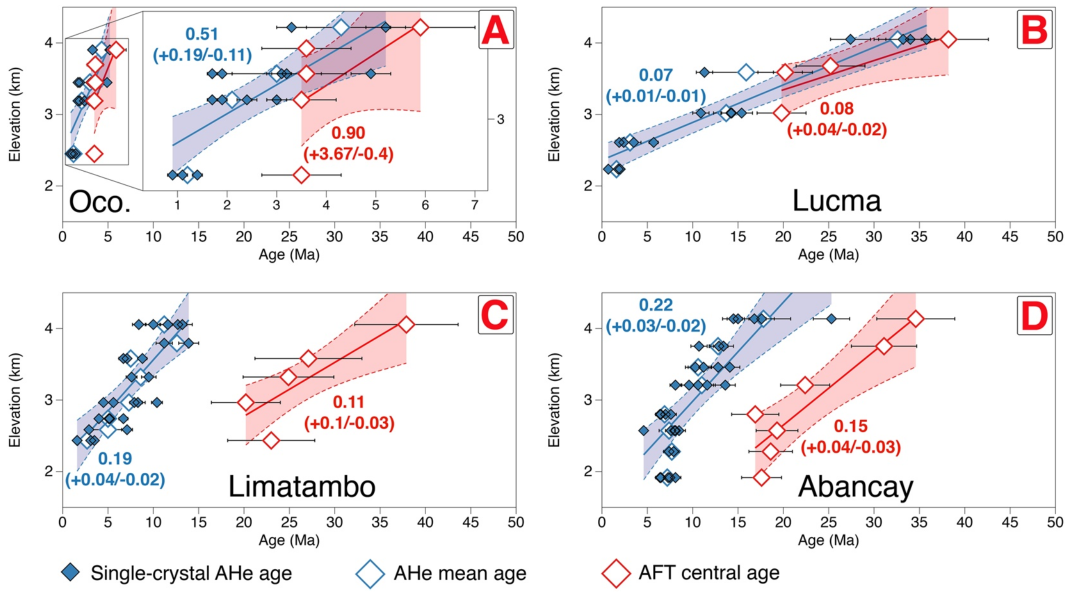

Figure 6. Age–elevation plots (AHe and AFT ages) for the vertical profiles of Ocobamba (A; Oco.), Lucma (B), Limatambo (C), and Abancay (D) (see Figure 4 for profiles location). Blue diamonds are single-grain AHe ages, open diamonds are mean AHe (blue), and central AFT (red) ages. Blue and red numbers on the graphics refer to AER apparent exhumation rates (km/Myr), respectively, for AHe and AFT ages. Blue and red dashed lines correspond to minimum and maximum values for exhumation rates (AER; 95% confidence interval). AHe, apatite (U–Th)/He; AFT, apatite fission track; AER, age–elevation relationship.

extracted the parameter value applying the 2σ standard deviation. We consequently used forward Pecube modeling to present the best fitting scenarios (*T*–*t* paths) and data reproducibility using inversion-derived parameters as input data (supporting information).

Because of computing time issues with the global model, and as the Altiplano and the Eastern Cordillera present opposite morphologies (flat vs. deeply incised; B. Gérard et al., 2021), and different exhumation trends according to local studies (slow and continuous [Ruiz et al., 2009] vs. recent acceleration [B. Gérard et al., 2021; Kennan, 2008]), we explored these areas separately with the ultimate goal to unravel their respective exhumation pattern. For the Altiplano model, we explored the basal crustal temperature (proxy for the geothermal gradient; Figure 5), the exhumation history for the entire crustal block (Figure 5), and landscape evolution through time (topography offset and relief amplification factor; Figure S38). Inverting topography offset and relief amplification factor can also be used to identify any potential reheating through sedimentary burial. If a complex cooling history with sample burial/reheating would be needed to explain the thermochronological data, we would expect the inversion outcomes to converge toward lowering of the relief amplification factor, implying valley filling and sample burial.

For the Eastern Cordillera model, we explored the exhumation history for the entire crustal block (Figure 5), relief and topographic evolution (Figure S38), and the kinematics of the Apurimac fault system (fault dip, timing of initiation, and fault velocity; Figure 5). Because of the code architecture, block exhumation and fault kinematics parameters were treated independently, which allows to explore both regional exhumation (spatially constant) and additional exhumation along the fault (spatially variable). For instance, the regional background exhumation (block exhumation) should imply deep-crustal/lithospheric mechanisms affecting equally the entire crustal block. The fault kinematics would imply a localized structure on which an additional source of exhumation could exist. Finally, the landscape dynamics through incision and deposition (relief and topographic evolution) could generate an additional source of exhumation or burial. Basal temperature for the Eastern Cordillera has been fixed in order to limit the number of inverted parameters and any modeling convergence issue. We fixed the basal temperature at 560°C (geothermal gradient of 18°C/km and surface temperature of 20°C) following previous studies (Barnes et al., 2008; Espurt et al., 2011; Henry & Pollack, 1988). This corresponds to an unperturbed geothermal gradient, which is then modified by rock

Table 2
Apatite (U–Th–Sm)/He Data

Sample number	Morphology	Length (μm)	Width (μm)	Thickness (μm)	R_s (μm)	Weight (μg)	F_T	^{4}He (nccSTP/g)	^{238}U (ppm)	^{232}Th (ppm)	^{147}Sm (ppm)	Th/U	eU (ppm)	Age (Ma)	Corrected age (Ma)	±1σ
Ocobamba profile																
AB-17-05A	2b	144	92	99	63	2.9	0.78	16,932	29.3	21.5	80.5	0.7	35	4.1	5.2	0.4
AB-17-05B	2py	201	128	115	61	4.1	0.77	14,156	40.5	25.2	84.6	0.6	47	2.5	3.3	0.3
AB-17-07A	1b + 1py	180	139	122	73	5.1	0.81	23,568	65.6	41.9	98.1	0.6	76	2.6	3.2	0.3
AB-17-07B	2b	118	125	79	54	2.1	0.74	22,253	45.1	26.1	93.4	0.6	52	3.6	4.9	0.4
AB-17-07C	2b	109	108	92	64	2.3	0.78	19,309	58.3	35.4	107.4	0.6	67	2.4	3.1	0.2
AB-17-07D	2b	194	128	115	79	6.2	0.82	7,087	36.2	26.3	92.8	0.7	43	1.4	1.7	0.1
AB-17-07E	1b + 1py	146	123	118	68	3.6	0.79	6,820	32.2	20.5	82.4	0.6	38	1.5	1.9	0.2
AB-17-08A	2b	198	112	114	76	5.8	0.81	12,131	63.8	29.1	88.9	0.5	71	1.4	1.7	0.1
AB-17-08B	1b + 1py	212	142	133	81	7.2	0.82	13,951	70.6	18.7	89.3	0.3	76	1.5	1.9	0.1
AB-17-08C	1b + 1py	168	117	122	69	4.2	0.80	14,539	56.3	27.4	85.2	0.5	63	1.9	2.4	0.2
AB-17-08D	1b + 1py	162	129	114	68	4.0	0.79	18,175	59.2	19.0	81.6	0.3	64	2.4	3.0	0.2
AB-17-08E	1b + 1py	182	164	157	89	7.7	0.84	8,668	47.2	17.1	72.9	0.4	52	1.4	1.7	0.1
AB-17-11A	1b + 1py	133	101	105	59	2.4	0.76	21,106	111.0	213.5	89.7	1.9	163	1.1	1.4	0.1
AB-17-11B	2b	171	99	93	64	3.5	0.78	13,654	65.5	157.8	72.5	2.4	104	1.1	1.4	0.1
AB-17-11C	1b + 1py	207	104	99	62	4.1	0.77	15,283	107.9	190.1	76.6	1.8	154	0.8	1.1	0.1
AB-17-11E	2b	191	119	99	69	4.7	0.79	3,626	29.4	55.0	27.3	1.9	43	0.7	0.9	0.1
Individual data																
AB-17-18A	2b	144	127	119	82	4.8	0.82	24,984	10.8	39.4	40.9	3.6	21	10.2	12.4	1.0
AB-17-18B	2b	146	93	96	63	2.9	0.78	42,585	19.6	68.4	52.4	3.5	36	9.8	12.7	1.0
AB-17-18C	2b	230	120	114	78	7.0	0.82	33,557	12.0	41.1	37.7	3.4	22	12.8	15.6	1.3
AB-17-18E	2b	128	128	99	69	3.2	0.79	20,493	8.3	27.5	35.9	3.3	15	11.4	14.4	1.2
AB-17-19A	2b	172	159	143	99	8.6	0.85	148,729	122.7	5.9	55.9	0.1	124	9.9	11.6	0.9
AB-17-19B	2b	158	129	93	65	3.7	0.78	108,144	103.9	11.9	48.2	0.1	107	8.4	10.7	0.9
AB-17-19I	2b	164	135	106	74	4.7	0.81	81,674	58.3	4.8	32.2	0.1	60	11.3	14.0	0.8
Lucma profile																
AB-17-21A	1b + 1py	169	126	112	68	4.1	0.79	5,878	50.8	144.1	61.4	2.8	86	0.6	0.7	0.1
AB-17-21C	2py	324	145	137	78	10.5	0.82	22,398	55.6	290.9	91.1	5.2	126	1.5	1.8	0.1
AB-17-21D	2b	207	141	118	82	7.2	0.82	10,613	35.4	102.9	40.6	2.9	60	1.5	1.8	0.1
AB-17-21E	1b + 1py	205	107	116	66	4.7	0.79	1,580	4.7	15.7	5.3	3.3	9	1.6	2.0	0.2
AB-17-22B	1b + 1py	205	100	98	61	3.9	0.77	109,443	72.5	16.5	83.3	0.2	77	11.8	15.4	1.2
AB-17-22C	2b	120	110	94	65	2.6	0.78	69,585	47.1	87.0	103.1	1.8	68	8.5	10.9	0.9
AB-17-22D	2b	130	119	108	74	3.6	0.81	89,394	60.5	14.5	71.9	0.2	64	11.5	14.3	1.1
AB-17-22E	1b + 1py	115	111	77	46	1.4	0.70	89,806	71.4	14.5	56.4	0.2	75	9.9	14.2	1.1

Table 2
Continued

Sample number	Morphology	Length (µm)	Width (µm)	Thickness (µm)	R_s (µm)	Weight (µg)	F_T	^{4}He (nccSTP/g)	^{238}U (ppm)	^{232}Th (ppm)	^{147}Sm (ppm)	Th/U	eU (ppm)	Age (Ma)	Corrected age (Ma)	±1σ
AB-17-25A	2b	102	137	84	56	2.0	0.75	129,728	39.0	3.5	80.0	0.1	40	26.9	35.8	2.9
AB-17-25C	2b	109	92	97	63	2.2	0.78	586,257	183.9	18.4	104.7	0.1	189	25.7	33.2	2.7
AB-17-25D	2b	145	125	80	54	2.6	0.74	266,746	82.9	19.7	93.8	0.2	88	25.2	34.0	2.7
AB-17-25E	1b + 1py	170	139	127	75	5.1	0.81	131,857	47.2	7.5	43.2	0.2	49	22.2	27.4	2.2
AB-17-26A	2b	217	111	105	72	5.6	0.80	37,130	17.4	5.0	67.6	0.3	19	16.4	20.5	1.6
AB-17-26C	2b	165	142	129	89	6.6	0.84	11,233	9.0	3.3	42.7	0.4	10	9.5	11.3	0.9
AB-17-28A	2py	218	94	84	49	2.8	0.72	15,300	40.8	142.5	69.7	3.5	75	1.7	2.4	0.2
AB-17-28B	2py	192	105	79	46	2.3	0.70	13,444	23.5	90.8	55.5	3.9	46	2.5	3.5	0.3
AB-17-28C	1b + 1py	228	117	89	57	4.1	0.75	11,401	34.8	125.5	57.5	3.6	65	1.5	1.9	0.2
AB-17-28D	2b	157	150	122	85	5.9	0.83	21,690	93.9	77.5	56.6	0.8	113	1.6	1.9	0.2
AB-17-28E	1b + 1py	146	101	94	57	2.4	0.75	31,059	31.3	121.4	59.5	3.9	61	4.3	5.7	0.5
Limatambo profile																
AB-17-29A	2b	173	109	100	69	4.1	0.79	46,518	37.9	83.0	7.5	2.2	58	6.7	8.4	0.7
AB-17-29B	2b	151	132	114	79	4.8	0.82	44,428	21.3	59.1	6.9	2.8	36	10.4	12.7	1.0
AB-17-29C	1b + 1py	165	92	89	54	2.5	0.74	37,896	19.2	54.1	11.9	2.8	32	9.8	13.2	1.1
AB-17-29D	1b + 1py	140	116	103	61	2.8	0.77	42,107	23.3	66.6	10.8	2.9	39	8.9	11.6	0.9
AB-17-29E	1b + 1py	149	110	112	64	3.2	0.78	19,662	13.4	31.7	8.7	2.4	21	7.8	10.0	0.8
AB-17-30B	1b + 1py	148	92	84	52	2.1	0.73	31,674	22.5	40.6	8.2	1.8	32	8.2	11.2	0.9
AB-17-30C	1b + 1py	170	133	104	64	3.8	0.78	29,403	14.2	35.4	8.8	2.5	23	10.8	13.9	1.1
AB-17-31A	2b	189	104	114	72	4.9	0.80	12,508	11.6	33.1	8.0	2.9	20	5.3	6.7	0.5
AB-17-31C	1b + 1py	153	112	99	60	2.9	0.77	10,929	11.0	23.3	4.8	2.1	17	5.5	7.1	0.4
AB-17-31E	1b + 1py	185	103	100	61	3.6	0.77	14,176	9.6	32.4	10.7	3.4	17	6.8	8.8	0.5
AB-17-32A	2b	140	114	103	71	3.6	0.80	12,686	9.6	32.4	4.5	3.4	17	6.1	7.6	0.6
AB-17-32B	2b	140	111	106	73	3.7	0.80	17,613	11.9	30.3	6.1	2.6	19	7.6	9.5	0.8
AB-17-33A	2py	155	109	100	50	2.2	0.72	8,244	7.4	19.0	7.0	2.6	12	5.7	7.9	0.5
AB-17-33B	1b + 1py	161	152	175	85	6.4	0.83	13,196	15.3	33.0	14.8	2.2	23	4.7	5.6	0.3
AB-17-33C	2b	175	115	102	71	4.5	0.80	19,221	36.9	31.1	5.6	0.8	44	3.6	4.5	0.3
AB-17-33D	1b + 1py	234	118	103	66	5.2	0.78	25,030	18.9	27.2	7.6	1.4	25	8.2	10.4	0.6
AB-17-33E	2b	133	119	104	72	3.5	0.80	13,308	11.2	21.8	11.5	1.9	16	6.7	8.3	0.5
AB-17-34A	2b	154	118	113	77	4.6	0.81	12,084	11.3	29.9	9.2	2.6	19	5.4	6.7	0.5
AB-17-34B	2b	155	152	126	87	6.2	0.84	7,372	7.6	27.1	7.7	3.6	14	4.4	5.2	0.4
AB-17-34C	2b	179	127	134	87	6.7	0.83	7,112	10.3	31.9	17.8	3.1	18	3.3	4.0	0.3
AB-17-34D	1b + 1py	139	93	95	55	2.2	0.75	5,905	8.1	19.5	5.5	2.4	13	3.8	5.1	0.4
AB-17-34E	2b	180	104	97	67	4.0	0.79	5,074	6.8	26.9	11.2	3.9	13	3.2	4.0	0.3

Table 2
Continued

Sample number	Morphology	Length (μm)	Width (μm)	Thickness (μm)	R_s (μm)	Weight (μg)	F_T	^{4}He (nccSTP/g)	^{238}U (ppm)	^{232}Th (ppm)	^{147}Sm (ppm)	Th/U	eU (ppm)	Age (Ma)	Corrected age (Ma)	±1σ
AB-17-35D	1b + 1py	203	122	97	62	4.1	0.77	5,720	15.3	25.9	8.9	1.7	22	2.2	2.9	0.2
AB-17-35E	2b	142	104	96	66	3.1	0.78	12,729	11.6	30.8	6.1	2.7	19	5.6	7.1	0.6
AB-17-36A	1b + 1py	142	103	105	60	2.7	0.77	9,698	23.5	41.8	8.5	1.8	34	2.4	3.1	0.3
AB-17-36D	1b + 1py	160	108	100	60	3.0	0.77	5,544	9.4	32.3	6.6	3.4	17	2.7	3.5	0.3
AB-17-36E	1b + 1py	186	128	123	74	5.2	0.81	3,274	12.6	37.8	10.5	3.0	22	1.3	1.6	0.1
Abancay profile																
AB-17-37A	2py	242	123	125	67	5.8	0.79	70,766	88.7	113.0	23.4	1.3	116	5.1	6.4	0.5
AB-17-37B	2b	117	113	102	70	2.9	0.80	72,471	82.8	104.3	22.2	1.3	108	5.6	7.0	0.6
AB-17-37C	1b + 1py	252	139	111	71	6.8	0.80	51,165	63.5	75.0	12.2	1.2	82	5.2	6.5	0.5
AB-17-37D	1b + 1py	189	132	100	57	3.5	0.75	38,099	44.3	45.9	18.3	1.0	56	5.7	7.6	0.6
AB-17-38A	1b + 1py	240	121	128	75	6.9	0.81	53,821	50.9	59.8	15.8	1.2	65	6.8	8.5	0.7
AB-17-38B	1b + 1py	254	132	144	82	8.8	0.83	52,415	52.3	56.4	16.8	1.1	66	6.6	8.0	0.6
AB-17-38C	2py	297	144	152	80	10.2	0.82	67,076	70.5	75.4	18.4	1.1	89	6.3	7.6	0.6
AB-17-38D	1b + 1py	260	133	149	83	9.3	0.83	77,615	74.9	87.9	19.9	1.2	96	6.7	8.1	0.6
AB-17-38E	1b + 1py	202	119	97	61	4.0	0.77	13,309	21.2	40.3	13.1	1.9	31	3.6	4.6	0.4
AB-17-39C	1b + 1py	190	129	132	77	5.8	0.81	55,767	61.8	41.0	27.6	0.7	72	6.4	7.9	0.6
AB-17-39D	2py	185	109	99	53	2.9	0.74	95,376	116.8	113.2	19.5	1.0	144	5.5	7.4	0.6
AB-17-40A	1b + 1py	237	118	124	73	6.6	0.81	137,948	171.0	73.7	33.9	0.4	189	6.1	7.5	0.6
AB-17-40B	2py	209	115	113	60	4.1	0.77	50,558	68.0	69.9	28.2	1.0	85	4.9	6.5	0.5
AB-17-40C	1b + 1py	247	128	137	79	8.0	0.82	92,739	112.4	67.5	28.2	0.6	129	6.0	7.3	0.6
AB-17-40D	2py	228	156	161	76	7.5	0.81	103,926	113.9	73.5	28.6	0.6	132	6.5	8.1	0.6
AB-17-40E	1b + 1py	197	128	104	65	4.5	0.78	49,030	70.7	42.0	14.7	0.6	81	5.0	6.4	0.5
AB-17-41A	1b + 1py	224	131	125	77	6.8	0.81	25,929	13.0	21.9	17.4	1.7	18	11.8	14.5	1.2
AB-17-41B	1b + 1py	115	103	95	55	1.8	0.74	50,384	18.0	17.6	10.3	1.0	22	18.8	25.3	2.0
AB-17-41C	2py	220	121	104	58	4.1	0.76	40,105	19.7	21.8	16.2	1.1	25	13.3	17.6	1.4
AB-17-41D	2b	160	111	134	77	4.9	0.81	27,300	10.1	26.9	17.6	2.7	17	13.7	16.8	1.3
AB-17-41E	1b + 1py	187	137	122	74	5.4	0.81	37,150	23.1	9.4	5.2	0.4	25	12.1	15.0	1.2
AB-17-42A	2b	180	128	122	83	6.3	0.83	67,778	44.1	34.7	13.7	0.8	52	10.7	12.9	1.0
AB-17-42B	2b	145	132	125	86	5.3	0.83	25,104	18.5	20.0	22.4	1.1	23	8.9	10.7	0.9
AB-17-42C	2py	216	109	113	59	4.1	0.76	100,130	68.3	52.9	14.8	0.8	81	10.2	13.4	1.1
AB-17-42D	1b + 1py	177	101	123	63	3.7	0.77	72,476	48.0	28.3	11.8	0.6	55	10.9	14.1	1.1
AB-17-43A	1b + 1py	166	108	90	56	2.8	0.75	49,427	40.8	7.3	12.7	0.2	43	9.6	12.8	1.0
AB-17-43C	2b	162	93	85	58	2.8	0.76	35,909	33.7	5.4	19.1	0.2	35	8.5	11.2	0.9
AB-17-43D	2b	197	92	100	63	3.9	0.77	49,624	45.3	25.0	20.1	0.6	52	8.0	10.3	0.8

Table 2
Continued

Sample number	Morphology	Length (μm)	Width (μm)	Thickness (μm)	R_s (μm)	Weight (μg)	F_T	^{4}He (nccSTP/g)	^{238}U (ppm)	^{232}Th (ppm)	^{147}Sm (ppm)	Th/U	eU (ppm)	Age (Ma)	Corrected age (Ma)	±1σ
AB-17-43E	2b	164	97	93	63	3.3	0.78	43,734	52.5	20.7	10.1	0.4	58	6.3	8.1	0.6
AB-17-44A	1b + 1py	214	112	101	63	4.5	0.78	144,444	129.5	14.1	13.7	0.1	133	9.0	11.6	0.9
AB-17-44B	1b + 1py	100	114	181	60	2.1	0.76	86,599	83.7	19.7	7.7	0.2	88	8.1	10.6	0.8
AB-17-44C	2b	184	139	114	79	6.0	0.82	76,257	76.9	12.9	9.1	0.2	80	7.9	9.6	0.8
AB-17-44D	1b + 1py	154	110	102	61	3.0	0.77	94,100	95.5	39.5	18.5	0.4	105	7.4	9.6	0.8
AB-17-44E	2b	136	110	110	74	3.7	0.81	134,264	88.5	52.8	17.6	0.6	101	11.0	13.6	1.1
Incahuasi profile																
AB-17-55A	1b + 1py	213	157	139	84	8.0	0.83	5,526	21.0	37.7	40.6	1.8	30	1.5	1.8	0.1
AB-17-55B	1b + 1py	198	117	110	68	4.7	0.79	6,030	28.8	47.5	47.3	1.6	40	1.2	1.6	0.1
AB-17-55C	2py	221	117	102	58	4.0	0.76	10,533	32.4	50.0	51.4	1.5	45	2.0	2.6	0.2
AB-17-55D	2b	183	129	125	85	6.6	0.83	5,988	21.5	36.6	52.4	1.7	31	1.6	2.0	0.2
AB-17-55E	1b + 1py	196	138	132	79	6.4	0.82	4,848	27.3	41.8	43.6	1.5	38	1.1	1.3	0.1

Note. Morphology refers to the apatite geometry. 2py, two hexagonal pyramids; 2b, two broken faces; 1b + 1py, one broken face and one hexagonal pyramid (Brown et al., 2013). F_T is the alpha-ejection correction factor and R_s is the sphere equivalent radius of hexagonal crystal (Gautheron et al., 2012; Ketcham et al., 2011).

advection. The detailed list of the explored Pecube parameters is available in Table S4.

4. Results

4.1. New Thermochronological Data and AERs

For the entire Abancay Deflection area, new 108 single-crystal AHe ages (from 28 samples) and 27 AFT central ages range from 0.7 ± 0.1 to 35.8 ± 2.9 Ma and from 2.6 ± 1.9 to 38.2 ± 4.4 Ma, respectively (Figures 4 and 6; Tables 2 and 3). Reproducibility of single-crystal AHe ages is satisfactory with averaged dispersion <10% for the whole data set. For AFT central ages, all samples passed the χ^2 test (>5%; Table 3 and Figures S1–S27), meaning that we can consider single-age populations for each sample (Green, 1981). Thermochronological ages ranging up to 40 Ma are characteristic of the northern Eastern Cordillera and the Altiplano, as shown for the Lucma, Abancay and Limatambo altitudinal profiles and individual data (AB-17-19 and AB-17-18; Figures 4 and 6). The southern Eastern Cordillera presents much younger thermochronological ages, all <10 Ma (Ocobamba profile and Incahuasi zone, AB-17-13 and AB-17-15; Figures 4 and 6).

For all altitudinal profiles, both AHe and AFT ages best fit a single AER statistically, but they reveal different rates and timing of exhumation (Figure 6). The Lucma profile presents apparent exhumation rates of $0.07^{+0.01}_{-0.01}$ and $0.08^{+0.04}_{-0.02}$ km/Myr since 40 Ma, based on AHe and AFT data, respectively (Figure 6), while the Abancay and Limatambo profiles give apparent exhumation rates between 0.1 to 0.2 km/Myr, with a possible increase in exhumation since 10–15 Ma (Figure 6). In the case of the Abancay profile, even if the three lowest samples appear aligned vertically (suggesting a potential acceleration in exhumation; Figure 6), our AER approach statistically favors a single linear trend, reconciled by the 95% confidence interval driven by data resolution and uncertainties. The Ocobamba profile presents much higher apparent exhumation rates for the last 6 Ma, with $0.5^{+0.2}_{-0.1}$ km/Myr based on AHe and $0.9^{+3.7}_{-0.4}$ km/Myr, based on AFT. These exhumation rates estimates correspond to the lowest computed BIC and consequently to the best fitting solutions according our Bayesian approach for interpreting AERs (Glotzbach et al., 2011).

4.2. Numerical Thermo(-Kinematic) Modeling

Modeled time–temperature (T–t) paths with QTQt show for the entire study area a moderate and continuous cooling history with a cooling rate of ~2.5 °C/Myr between 40 Ma (~38 Ma for the Limatambo profile due to the intrusion emplacement constraint; Figure 7c) and ca. 5 Ma (Figure 7; note that the rapid cooling for the Limatambo profile is due to the Cotabamba pluton crystallization and has not been taking into account because it has a very limited effect over time). Whereas cooling trends are relatively similar for the northern Eastern Cordillera and the Altiplano (Figures 7a, 7c, and S31–S35), T–t paths for the southern Eastern Cordillera (Ocobamba profile and individual data) suggest an increase in cooling rate with values of ~17°C/Myr between 7 and 3 Ma (Figures 7b, S28–S30, and S36), in agreement with AERs (Figure 6). It appears, however, that the timing for cooling acceleration in the Incahuasi zone (Figures 4 and S36) occurred slightly later (2–3 Ma). This signal could correspond to the same cooling acceleration identified for the southern Eastern Cordillera (7–3 Ma) with a short time-lag, or, could represent a local trend due to unidentified fault and/or exhumation process. Individual QTQt-derived cooling paths (Figures S28–S36) exhibit short-term variations and more complex possible thermal histories. For a conservative approach, we chose to extract the statistically most robust signal for each profile or individual sample, by considering the 95% confidence interval around the expected *T*–*t* path (Figure 7). This method prevents from potential overinterpretation of model outcomes, by focusing on well-constrained *T*–*t* paths. The apparent cooling increase at <2 Ma observed for Lucma and Limatambo profiles (Figures S33 and S34) represents a modeling bias. Indeed, all samples are colder than the closure temperature. The present-day surface temperature imposed in QTQt drives this apparent cooling acceleration, not supported by the thermochronological data. These modeling biases are not further considered in the following.

For Pecube modeling, we display results from our thermokinematic inversions in 2D graphs, where the explored parameter space is illustrated and each forward model is colored by its respective misfit value (Figures 8 and 9). We present thereafter the best fitting value for explored parameters within each modeled crustal block. For the Altiplano model, parameter exploration through data inversion reveals a clear inversion convergence for the output background exhumation rate at 0.2 ± 0.1 km/Myr (Figure 8a) with high reproducibility of observed thermochronological ages and time–temperature paths (Figures 8b and S41). The basal temperature does not converge but presents four peaks at 420°C ± 15°C, 480°C ± 20°C, 525°C ± 10°C, and 675°C ± 30°C (Figure 8a) corresponding, respectively, to geothermal gradients of 14 ± 1, 16 ± 1, 17 ± 1, and 22 ± 1°C/km (Text S1). Relief amplification factors do not converge neither and are nondeterminative or not discriminating (Figure S39). For the Eastern Cordillera model, the well-constrained value for background exhumation is converging to 0.2 ± 0.1 km/Myr (Figure 9a), similarly to the Altiplano results. The lateral (north-south) position of the Apurimac fault system at 25-km depth (x fault parameter) is constrained to −34 ± 5 km (the negative sign corresponds to the northward exploration of this parameter). According to the approximate surface trace of the Apurimac fault system and to the output value for x fault, we estimated a fault dip ranging between 28° and 47° toward the north (Figures 9a and 9d). Regarding the fault kinematics, Pecube models favor fault activation at 5.3 ± 1.5 Ma with an associated fault velocity of 2.9 ± 0.6 km/Myr (Figure 9b). By taking into account the fault dip and velocity predictions, fault-induced exhumation rate is ~1 km/Myr. By adding background exhumation to the previous results, net exhumation rates of 1.2 ± 0.4 km/Myr are predicted for the southern Eastern Cordillera since ~5 Ma (Figure 9e). For the same time period, the northern Eastern Cordillera and the Altiplano underwent steady exhumation rates (Figure 10). Finally, and similarly to the Altiplano crustal-block model, relief amplification factor through time does not converge for the Eastern Cordillera model (Figure S40). The thermochronological data reproducibility is, however, robust (Figure S42).

5. Discussion

5.1. From Cooling Rate to Exhumation Rate

Our three different and independent modeling approaches are based on the statistically most robust scenarios for cooling and exhumation. As a result, they may not entirely reflect the variability of raw thermochronological data. Such an approach is, however, conservative to interpret models without overinterpreting the outcomes. Because the landscape parameters (topography offset and relief amplification factor) did not converge for Pecube inversions, the landscape evolution through time cannot be quantitatively assessed by our modeling. The relief amplification factor (Figure S38) can be used as a proxy for burial, that is, reheating of the upper crust. As shown by the nonconvergence toward a minimization of the relief amplification factor at any time step explored (Figures S39 and S40), Pecube inversions confirm that no burial/reheating is required to accurately reproduce the thermochronological data set. This result implies that the thermal perturbation supposedly associated with the magmatic arc activity between 50 and 30 Ma (Mamani et al., 2010) is not registered in our local thermochronological record (except maybe for the highest and oldest AFT data from the Limatambo profile). This can be explained by three reasons: (1) present-day outcropping rocks were at that time still at depth and thus at temperatures above the PRZ/PAZ, that is, not impacted

Table 3
Apatite Fission Track Data

Sample number	n	ρ_s (10^5 cm^{-2})	N_s	ρ_i (10^5 cm^{-2})	N_i	ρ_d (10^5 cm^{-2})	$P(\chi^2)$	Dispersion (%)	Central age (Ma)	$\pm 2\sigma$	U (ppm)	$\pm 1\sigma$	n D_{par}	MDpar (µm)	n TL	MTL (µm)
Ocobamba profile																
AB-17-05	23	0.99	140	27.7	3,915	12.0	100.0	0.0	5.9	1.1	35	2	88	1.09	6	11.43
AB-17-06	24	0.47	69	21.3	3,155	12.0	99.3	0.1	3.6	0.9	27	1	82	1.12	3	12.34
AB-17-07	22	0.64	90	29.2	4,098	12.0	84.6	0.4	3.6	0.8	36	1	68	1.27	5	10.92
AB-17-08	25	0.85	136	40.6	6,486	12.0	93.6	0.2	3.5	0.7	51	2	106	1.16	12	11.48
AB-17-11	20	0.73	79	34.3	3,725	12.1	99.7	0.1	3.5	0.8	43	2	96	1.30	1	9.8
Individual data																
AB-17-13	30	0.65	106	18.3	3,007	12.1	100.0	0.0	5.9	1.3	23	1	66	1.24	5	10.76
AB-17-15	26	0.07	9	4.15	568	12.1	99.3	0.2	2.6	1.9	5	0	52	1.18	N.D.[a]	N.D.[a]
AB-17-18	25	1.01	160	6.82	1,081	12.1	100.0	0.1	24.7	4.6	8	1	109	1.53	3	10.83
AB-17-19	25	4.32	476	34.2	3,762	12.2	87.0	0.3	21.1	2.7	42	2	139	1.29	10	11.48
Lucma profile																
AB-17-22	22	3.98	388	33.7	3,285	12.2	87.1	0.3	19.8	2.7	41	2	115	1.15	5	10.87
AB-17-23	18	6.79	314	46.4	2,090	12.2	47.4	6.9	25.2	3.8	57	3	92	1.16	7	11.72
AB-17-25	18	16.5	901	73.0	3,979	12.3	51.7	4.0	38.2	4.4	89	3	121	1.80	7	13.59
AB-17-26	24	2.95	286	24.8	2,393	12.3	99.9	0.1	20.2	3.0	30	1	117	1.21	7	11.64
Limatambo profile																
AB-17-29	19	4.97	307	24.8	1,532	13.8	96.0	0.1	37.9	5.7	27	2	96	1.65	8	11.99
AB-17-31	20	1.52	109	10.6	764	13.8	94.6	0.3	27.1	5.9	12	1	116	1.32	3	12.15
AB-17-32	20	1.90	133	14.5	1,017	13.9	98.5	0.1	24.9	5.0	16	1	151	1.42	2	11.69
AB-17-33	22	1.87	159	17.6	1,499	13.9	93.1	0.2	20.2	3.8	19	1	117	1.19	3	12.46
AB-17-36	18	1.95	120	16.3	1,000	14.0	66.4	0.6	23.0	4.8	17	1	70	1.30	3	10.68
Abancay profile																
AB-17-37	20	4.44	244	50.6	2,778	14.0	100.0	0.1	16.9	2.6	54	2	103	1.24	3	12.10
AB-17-38	20	6.94	647	69.4	6,470	14.0	100.0	0.0	19.3	2.3	74	2	113	2.15	18	12.43
AB-17-39	20	4.77	506	49.6	5,262	14.1	99.9	0.1	18.6	2.4	53	2	102	1.57	5	11.38
AB-17-40	20	5.73	532	62.9	5,837	14.1	92.2	0.1	17.6	2.2	67	2	80	1.47	7	10.94
AB-17-41	26	3.27	544	18.3	3,041	14.1	99.9	0.1	34.6	4.3	19	1	118	1.42	N.D.[a]	N.D.[a]
AB-17-42	26	5.48	764	34.1	4,761	14.1	87.2	0.6	31.1	3.6	36	1	137	1.46	7	11.72
AB-17-44	25	5.15	632	44.6	5,477	14.2	98.1	0.2	22.4	2.7	47	2	146	1.70	21	11.37
Incahuasi profile																
AB-17-51	14	0.45	18	9.66	389	14.2	12.7	44.0	9.0	5.2	10	1	32	1.41	N.D.[a]	N.D.[a]
AB-17-55	27	0.88	64	25.1	1,833	14.2	9.0	39.1	6.6	2.1	26	1	108	0.98	6	10.71
Previous studies																
LK95/200[b]	30	N.R.[c]	N.R.[c]	N.R.[c]	N.R.[c]	N.R.[c]	46.5	N.R.[c]	2.2	0.5	N.R.[c]	N.R.[c]	N.R.[c]	N.R.[c]	N.R.[c]	N.R.[c]
LK95/202[b]	30	N.R.[c]	N.R.[c]	N.R.[c]	N.R.[c]	N.R.[c]	97.0	N.R.[c]	2.4	0.5	N.R.[c]	N.R.[c]	N.R.[c]	N.R.[c]	N.R.[c]	N.R.[c]
Pi6.1[d]	23	2.27	456	20.7	4,159	11.0	10.0	N.R.[c]	22.5	N.R.[c]	23	2	40	2.68	41	11.21
Pi6.2[d]	16	1.55	168	13.8	1,491	10.9	100.0	N.R.[c]	22.0	N.R.[c]	17	2	20	2.78	31	13.40
Pi6.3[d]	20	1.74	323	16.2	3,005	10.8	99.5	N.R.[c]	20.8	N.R.[c]	18	1	44	2.87	37	14.04
Pi6.4[d]	20	0.69	137	6.21	1,242	10.7	98.0	N.R.[c]	21.1	N.R.[c]	7	2	28	2.37	46	12.76
Pi6.5[d]	19	0.79	148	9.05	1,701	10.6	100.0	N.R.[c]	16.5	N.R.[c]	10	2	43	2.55	34	13.13

10.1029/2020TC006314

Table 3
Continued

Sample number	n	ρ_s (10^5 cm^{-2})	N_s	ρ_i (10^5 cm^{-2})	N_i	ρ_d (10^5 cm^{-2})	$P(\chi^2)$	Dispersion (%)	Central age (Ma)	$\pm 2\sigma$	U (ppm)	$\pm 1\sigma$	n D_{par}	MDpar (µm)	n TL	MTL (µm)
Pi6.6[d]	20	1.04	203	12.0	2,354	10.5	87.0	N.R.[c]	16.2	N.R.[c]	14	1	31	2.61	21	13.36
Pi6.7[d]	20	1.09	141	12.7	1,637	10.4	93.0	N.R.[c]	16.0	N.R.[c]	16	2	23	2.72	35	12.89
Pi6.8[d]	20	0.86	140	10.2	1,662	10.3	93.0	N.R.[c]	15.5	N.R.[c]	12	2	17	2.98	30	12.45

Note. Fission track age is given as Central Age (Galbraith & Laslett, 1993). Tracks were counted and horizontally confined track lengths were measured dry at 1,250X magnification under an Olympus BX51 optical microscope, using the FTStage 4.04 program at ISTerre. Ages were calculated with the BINOMFIT program (Ehlers et al., 2005), using a zeta value of 275.18 ± 11.53 and the IRMM 540 uranium glass standard (15 ppm U). MDpar = mean Dpar value, MTL = mean track lengths of horizontally confined tracks.

[a]N.D. = no data. [b]Previous data (Kennan, 2008). For samples LK95/200 and LK95/202, elevations are respectively 3.1 and 2.1 km. [c]N.R. = not reported. [d]Previous data from Ruiz et al. (2009) for samples Pi6.1 (3.87 km), Pi6.2 (3.80 km), Pi6.3 (3.65 km), Pi6.4 (3.45 km), Pi6.5 (3.25 km), Pi6.6 (3.10 km), Pi6.7 (3.00 km), and Pi6.8 (2.85 km).

by this reheating event; (2) for the southern Eastern Cordillera, the high exhumation rates since ~5 Ma have removed the upper crustal section that could have potentially registered older thermal perturbations; and (3) the thermal perturbation was potentially spatially and/or temporally localized and did not affect our sampled sites. This last point also applies for the 7–0.5 Ma volcanism along the Apurimac fault system described south of Cuzco and in northern Bolivia by Bonhomme et al. (1988). The volcanism was spatially localized and spread out sporadically over time. The thermal perturbation induced was thus restricted to the Apurimac fault zone, limited in time, and did not affect our sample sites. The same reasoning applies to a potential sediment burial that could have affected the Altiplano. We consequently assumed that our samples did not experienced reheating after 40 Ma. Modeled thermal histories obtained from the Abancay Deflection area present only a monotonic cooling phase with variable cooling rates (Figure 7). This simplifies our modeling approach regarding the crustal thermal structure.

Because we did not detect any perturbation of thermal histories by reheating or potential isotherm relaxation (sampled rocks were deep and hot enough before the modeled onset time for rock cooling), we convert the inferred cooling scenario into simple exhumation histories. Exhumation rates estimated from QTQt-derived cooling rates and using a steady and spatially uniform geothermal gradient (18 ± 4°C/km), apparent exhumation rates from AERs (Glotzbach et al., 2011), and Pecube inversions results are all consistent with high data reproducibility between three independent approaches (Figure S43). This confirms that the assumed geothermal gradients for QTQt and Pecube models are satisfactory, even if we cannot tightly constrain the basal crustal temperature from Pecube inversion (Figure 8a). This nonconvergence issue is frequently encountered in this type of modeling (e.g., Robert et al., 2011; Valla et al., 2012) and can be bypassed only by imposing thermal parameter values from regional estimates. In detail, we identified four temperature peaks (probability density function for the Altiplano model; Figure 8a), corresponding to geothermal gradients spanning from 13 to 23°C/km, compatible with our chosen value of 18 ± 4°C/km for the uppermost 5 km of the crust, using a basal temperature of 560°C. We furthermore performed inversion for each crustal model (Altiplano and Eastern Cordillera blocks; Table S4; Text S5), imposing a "warmer" geothermal gradient (30°C/km; Text S5). It clearly appears that the ~20°C/km geothermal gradient seems to be the most likely option for the Abancay Deflection at the scale of our study, with better thermochronological data reproducibility (Text S5; Figures S45 and S46).

We separated the study area into three zones derived from the patterns in output exhumation rate (QTQt; Figures 4 and 7). Using Pecube outcomes, the Altiplano and the northern Eastern Cordillera experienced similar exhumation histories since 40 Ma with exhumation rates of 0.15 ± 0.10 km/Myr (Figure 10). The southern Eastern Cordillera experienced the same exhumation rate from ~20 to 5.3 ± 1.5 Ma, followed by an acceleration of exhumation to 1.2 ± 0.4 km/Myr (Figure 10). Even though the thermochronological data modeling and output time–temperature paths from QTQt are limited to the last 20 Ma for the southern Abancay Deflection (Figures 7b and 9c), we propose by temporal extrapolation that the southern Eastern Cordillera underwent similar exhumation rates as its neighboring areas (i.e., Altiplano and northern

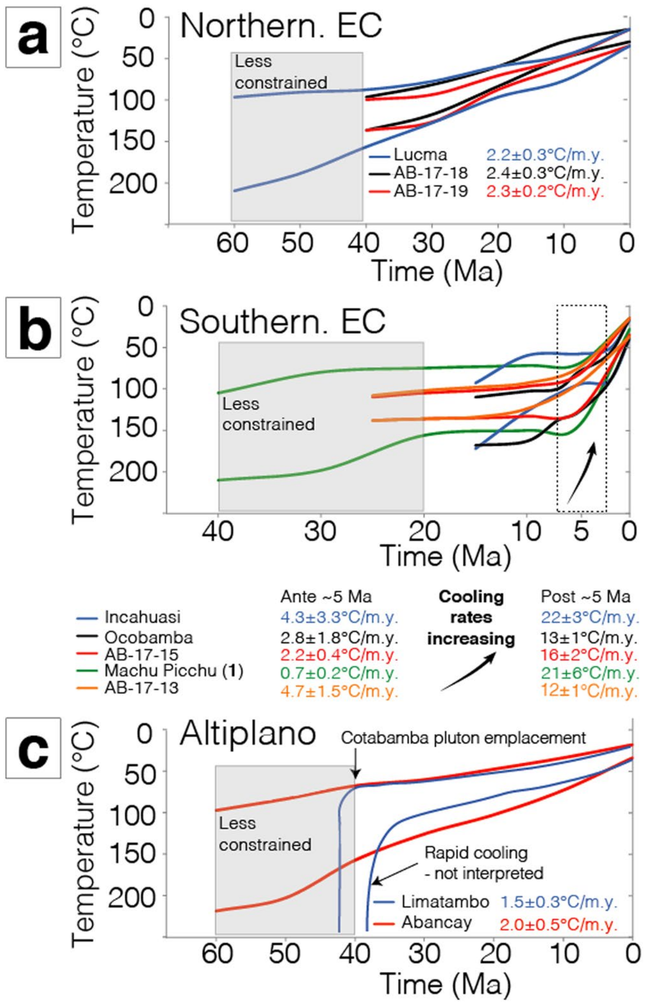

Figure 7. Time–temperature paths derived from QTQt inverse modeling of thermochronological data (Gallagher, 2012). (a–c) Synthesis of time–temperature paths (colored lines) derived from QTQt (95% confidence interval around the expected model; see the supporting information for detailed inverse modeling outcomes). For profiles, because cooling dynamics are similar for top and bottom samples we plotted here the minimum and maximum confidence envelops. Colored numbers in legend refer to the output cooling rates. See the supporting information for details regarding the data reproducibility (observed vs. predicted data). (a), (b), and (c), respectively, correspond to samples in the northern Eastern Cordillera (EC), the southern Eastern Cordillera, and the Altiplano (see Figure 4 for location). In (b), number 1 (Machu Picchu profile) refers to B. Gérard et al. (2021) and the black dotted rectangle corresponds to the cooling acceleration timing at 5 ± 2 Ma.

Eastern Cordillera) between 40 and 20 Ma. We proposed this hypothesis because no data corroborate any incision and/or tectonic activity pulses that would modify the exhumation dynamics affecting the southern Eastern Cordillera, punched between the northern Eastern Cordillera and the Altiplano. Over the last ~5 Ma, the exhumation acceleration is spatially framed southward by the Apurimac fault system, pointing toward a differential exhumation pattern in the Abancay Deflection that we attribute to tectonically driven rock uplift along the Apurimac fault system with rock removal by efficient erosion.

5.2. Exhumation of the Abancay Deflection Between 40 and 5 Ma

The whole Abancay Deflection region experienced steady, moderate (0.2 ± 0.1 km/Myr) and apparently spatially uniform exhumation between 40 and 5 Ma (Figures 10 and 11). This exhumation rate is highly consistent with those inferred between 40 and 15 Ma from the only thermochronological data available in the area (0.17 km/Myr; Ruiz et al., 2009). Even if the Peruvian Altiplano experienced Miocene faulting delimitating intramountainous basins (Tinajani, Punacancha, and Paruro basins; Carlotto, 2013; Horton et al., 2014), there is no evidence for any acceleration of exhumation nor sedimentary burial related to these crustal processes according to our three independent modeling approaches. Surprisingly, although the Bolivian Eastern Cordillera registered peaks of exhumation through tectonic and erosional processes between 50 and 15 Ma (Barnes et al., 2012; ~500 km to the south-east of our study area), our data and inverse models rather favor a large-scale uniform exhumation history during that period.

Consequently, we interpret the steady and uniform exhumation rates as the record of low-magnitude surface denudation affecting the Abancay Deflection in an internally drained environment (Figure 11; B. Gérard et al., 2021). Furthermore, contemporaneously to the Bolivian Orocline bending during Miocene (Roperch et al., 2006), the Abancay Deflection was built in a left-lateral transpressional context (Dalmayrac et al., 1980) associated with lateral rock advection from the south (Figures 11c and 11d) with limited rock uplift as shown by QTQt and Pecube inversions (Figure 9c); that is, data reproducibility is overall good without implying any additional earlier rock uplift due to the transpressional context. The crustal tectonic regime, dominated by horizontal motion, cannot be registered by the thermochronological data, nor easily modeled by balanced cross section that encompass only 2D processes (Gotberg et al., 2010). Moreover, our outcomes, pointing toward a low-magnitude exhumation rate of ~0.2 km/Myr between 40 and 5 Ma, are comparable in terms of magnitude with the large-scale and steady surface uplift (at ~0.1 km/Myr) of the Eastern Cordillera and the Altiplano modeled by Sundell et al. (2019). The output exhumation rates are the part of rock uplift accommodated by erosion, while the remaining part (unconstrained by our thermochronological record) is the surface uplift.

The low-exhumation and surface-uplift rates are compatible with large-scale tectonic shortening (Lamb, 2011; Phillips et al., 2012) and/or lower crustal flow (Husson & Sempere, 2003; Ouimet & Cook, 2010; Tassara, 2005). Kar et al. (2016) suggested more rapid surface uplift of the northern Altiplano between 10 and 5 Ma (0.4 km/Myr). Indeed, one or multiple lithospheric delamination event(s) implying pulses of rapid surface uplift have been proposed during the Miocene (Garzione et al., 2017). Consequently, the Altiplano may have risen rapidly without prominent incision and thus recorded limited exhumation (i.e., steady

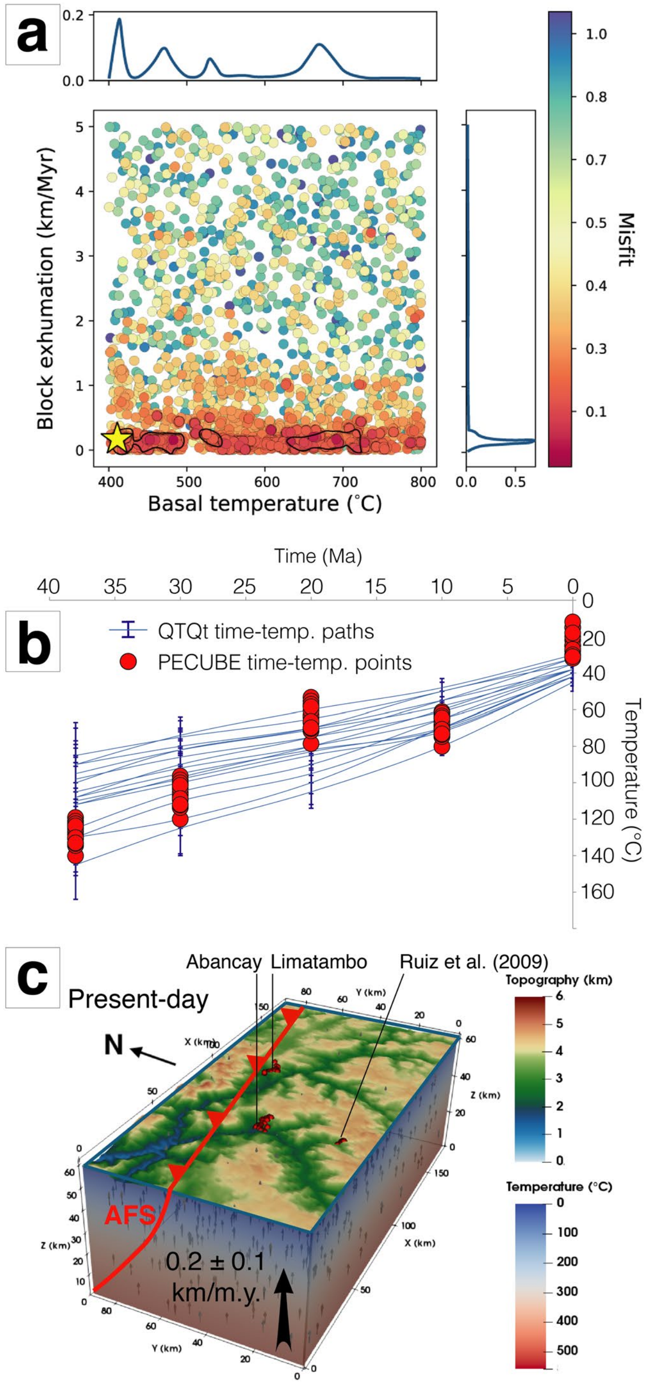

Figure 8. 3D Pecube inversion results for the Altiplano crustal block. (a) 2D parameter space and inversion results for crustal-block exhumation versus basal temperature. Each colored point corresponds to one forward model. Blue curves (up and right subpanels) are the probability density for each parameter. The yellow star is the best fitting model. (b) Direct comparison of time–temperature paths derived from QTQt and ones computed with Pecube best fitting model. (c) Crustal-block model for the Altiplano (see Figure 2 for location) with locations of thermochronological data.

low-exhumation rates despite rapid surface uplift). In a potentially endorheic context (B. Gérard et al., 2021), sediment evacuation and thus large-scale erosion rates are low. Such an acceleration of surface uplift should have induced an increase in erosion/exhumation via enhanced erosion due to orographic precipitation, at the edge of the plateau between 10 and 5 Ma. Nevertheless, it has been also demonstrated from regional-climate numerical modeling that such a surface-uplift acceleration can be an artifact driven by climatic variability (Ehlers & Poulsen, 2009). Considering our data and modeling outcomes, as well as the timing of the exhumation acceleration from our data (5 ± 2 Ma), we cannot discard nor validate any of these surface-uplift models (slow and steady vs. acceleration of surface uplift between 10 and 5 Ma).

5.3. Southern Eastern Cordillera: 5 Ma Exhumation Rate Increase

The southern Eastern Cordillera, framed southward by the Apurimac fault system, has registered an order-of-magnitude acceleration in exhumation since ca. 5 Ma, driven by both topographic incision and tectonic uplift. The capture of an endorheic high-elevation paleo-Altiplano and subsequent pulse of incision could partly explain the exhumation acceleration for the southern Eastern Cordillera, although not enough to explain the total amount of exhumation since 5 Ma (B. Gérard et al., 2021). This timing is consistent with the inferred initiation of canyon carving (Pliocene) further south in the Bolivian Eastern Cordillera (Lease & Ehlers, 2013). Pecube modeling, however, does not allow quantitatively constraining relief and topographic evolution through time (Text S4).

The local 5-Ma exhumation event affecting the southern Eastern Cordillera (Figure 11e) cannot be explained by large-scale phenomenon such as lithospheric delamination, neither in terms of spatial extent nor timing (Garzione et al., 2006; Sobolev & Babeyko, 2005). Tectonic uplift along local structures associated with enhanced erosion could be a potential trigger for our observed pattern of thermochronological ages and exhumation (Figures 4, 6, and 7). Pecube inverse outcomes show that the inherited crustal-scale Apurimac fault system can reproduce the 3D thermochronological data pattern, with significant tilting of the southern Eastern Cordillera (Figure 9). Regionally, the fault system is curved around the Abancay Deflection. In such a deflected thrusting pattern, it is geometrically difficult to link the southern Eastern Cordillera to a south-dipping ramp located beneath and connected to the main Subandean front without implying an unlikely and complex structural geometry. Furthermore, the Subandean front has been active since 14 Ma (Espurt et al., 2011), which clearly predates the 5-Ma exhumation signal we observed in the Eastern Cordillera. The Apurimac fault system appears to be the most likely structure tilting the Eastern Cordillera (Figure 9) associated with backthrusting activity with a relatively low north-dipping angle of 30°–40° (Figure 9d). This tectonic signal is added to the large-scale and long-term exhumation signal affecting the whole area since 40 Ma (0.2 ± 0.1 km/Myr) and generates the differential exhumation pattern observed in Figure 9e.

Considering end-member values of best fitting Pecube parameters (i.e., fault dipping angle, timing for fault activation, and fault velocity), we estimated a first-order total horizontal crustal shortening ranging be-

10.1029/2020TC006314

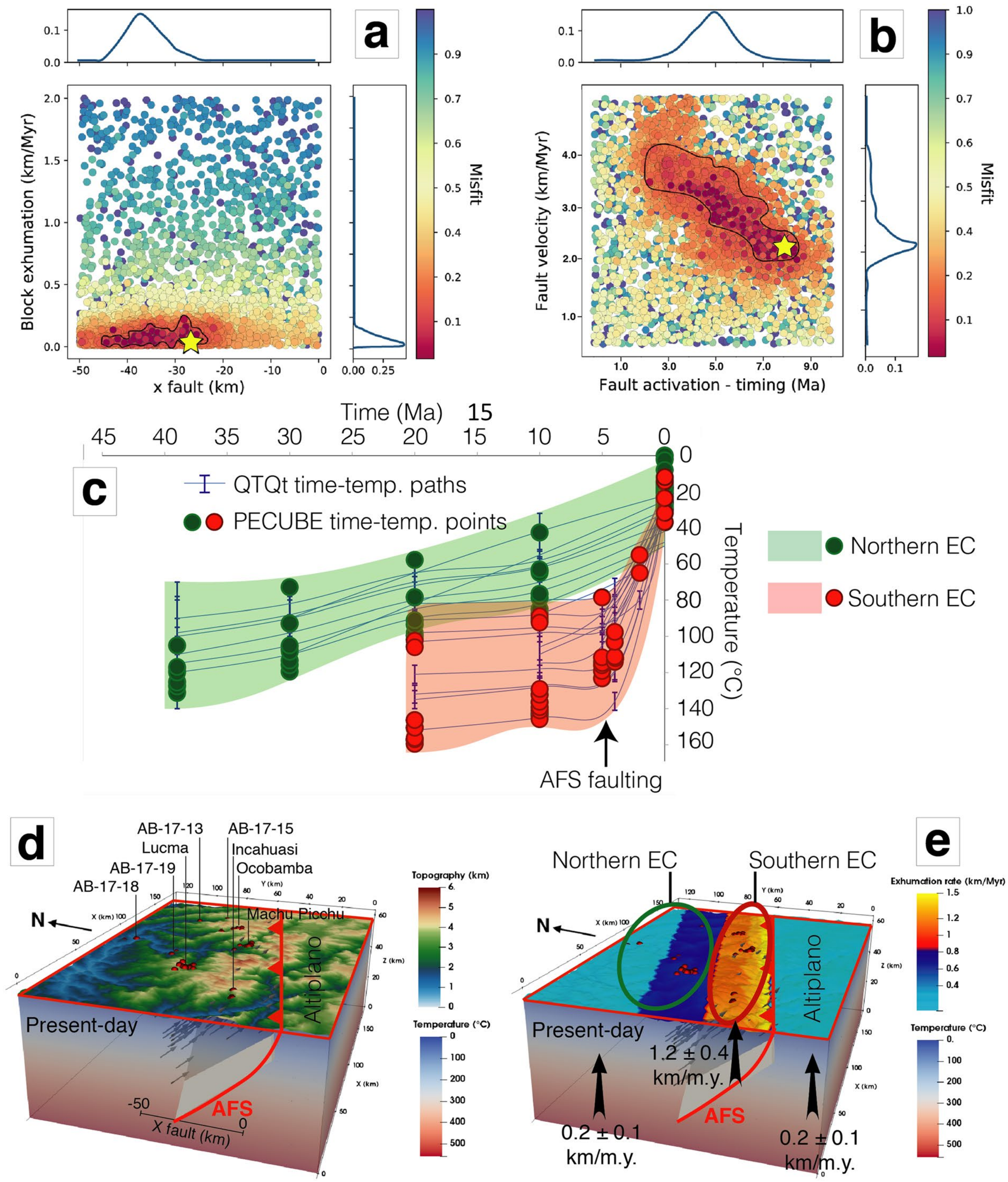

Figure 9. 3D Pecube inversion results for the Eastern Cordillera crustal block. (a) 2D parameter space and inversion results for crustal-block exhumation versus position of the fault at 25-km depth (x fault parameter). (b) 2D parameter space and inversion results for the fault velocity versus activation timing of the Apurimac fault system. Each colored point corresponds to one forward model. Blue curves (up and right subpanels) are the probability density for each parameter. The yellow stars in (a) and (b) are the best fitting model. (c) Direct comparison of time–temperature paths derived from QTQt and ones computed with Pecube best fitting model. (d) Crustal-block model for the Eastern Cordillera with locations of thermochronological data (see Figure 2 for location). (e) Surface exhumation pattern for the Eastern Cordillera since ~5 Ma predicted from Pecube best fitting model. AFS is the Apurimac fault system.

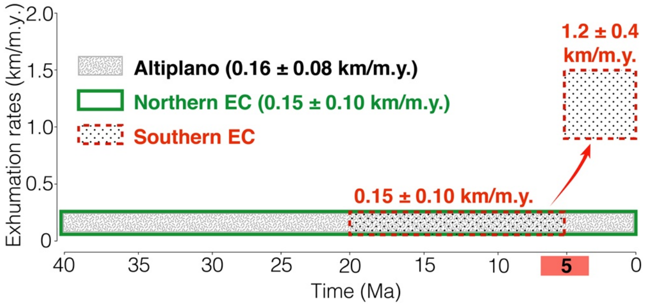

Figure 10. Exhumation rates derived from Pecube for the Abancay Deflection through time. Each color corresponds to the three exhumation areas identified in this study. Details regarding the computed values for exhumation rates according to AERs, QTQt, and Pecube are available in Figure S43. AER, age–elevation relationship.

tween 6 and 21 km (mean shortening rate of 2.8 ± 1.5 km/Myr). The total amount of vertical rock uplift ranges between 4 and 17 km (mean rock-uplift rate of 2.2 ± 1.3 km/Myr) since 5 Ma. However, given our thermochronometric data set and the lack of high-temperature thermochronometers to further constrain the pre-5-Ma exhumation in the area, we considered that highest rock uplift estimated from Pecube modeling are unrealistic and rather should be ~7 km maximum for the last 5 Ma. The parameter ranges derived from our approach do not allow to constrain precisely the tectonic deformation (nor vertical or horizontal) rates and thus to further discriminate the tectonic balance and the respective importance of different rock-uplift drivers for the southern Eastern Cordillera. On the other hand, rock-uplift rates overlap with exhumation rates over the last 5 Ma (2.2 ± 1.3 km/Myr vs. 1.2 ± 0.4 km/Myr, respectively; Figure 10), which highlights the consistency between 2D and 3D modeling approaches. Furthermore, constrained 5-Ma horizontal shortening rates for the southern Eastern Cordillera (2.8 ± 1.5 km/Myr) are also consistent with balanced cross-section reconstructions and derived shortening rates in the Subandean area (~3.8 km/Myr; Espurt et al., 2011), directly located to the north of the Abancay Deflection (Figure 1).

Although thick-skinned backthrusts have been reported as active since the late Miocene to the north of the Abancay Deflection (Shira mountains; Gautheron et al., 2013; Huaytapallana fault, in the continuity of the Apurimac fault system; Dorbath et al., 1990, Figure 3b), we document for the first time the recent tectonic activity (i.e., <5 Ma) for the Abancay region itself, with significant but local exhumation along the Apurimac fault system south-verging backthrusting. The low-magnitude earthquake cluster in this zone

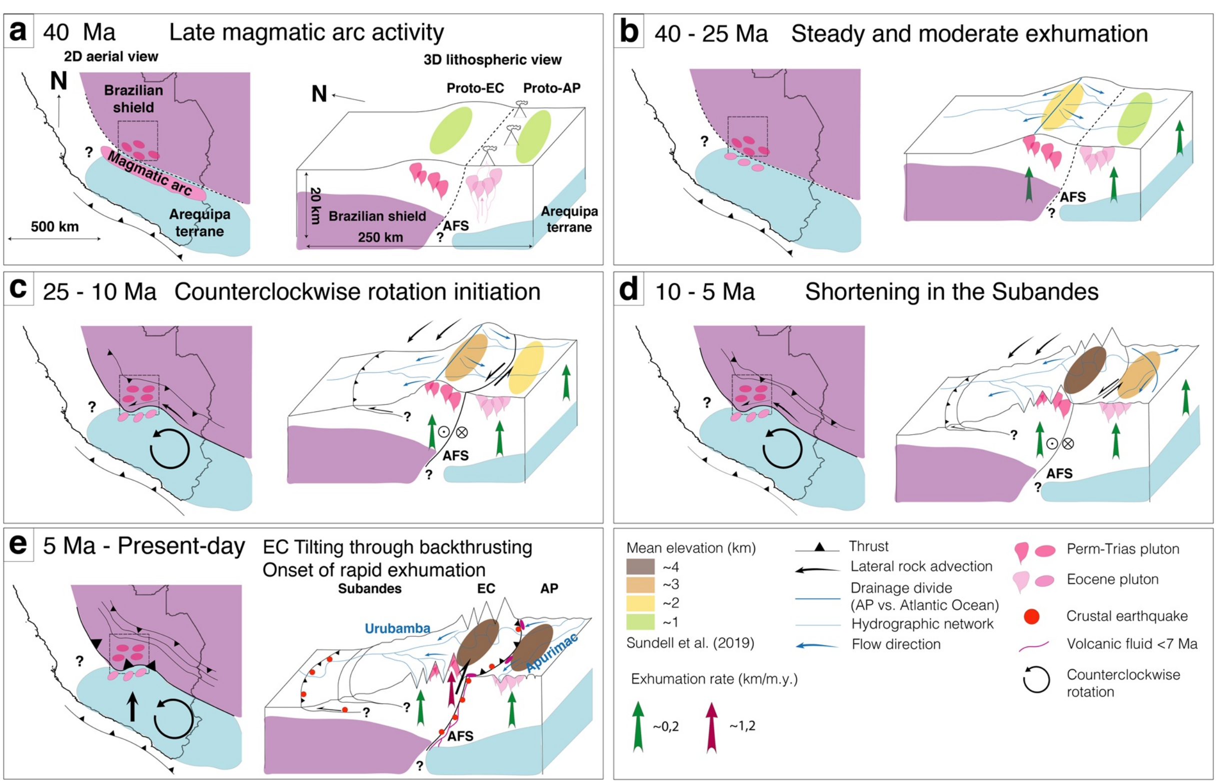

Figure 11. Tectonomorphic evolution of the Abancay Deflection since 40 Ma. Left panels represent the large-scale schematic map views of the study area (black dashed square). Right panels are 3D Abancay Deflection schematic crustal blocks corresponding to the surface to the square defined in the left panels. (a), (b), (c), (d), and (e) refer, respectively, to the situation at 40 Ma, between 40 and 25 Ma, between 25 and 10 Ma, between 10 and 5 Ma, and finally since 5 Ma to present day. AFS, Apurimac fault system; AP, Altiplano; EC, Eastern Cordillera.

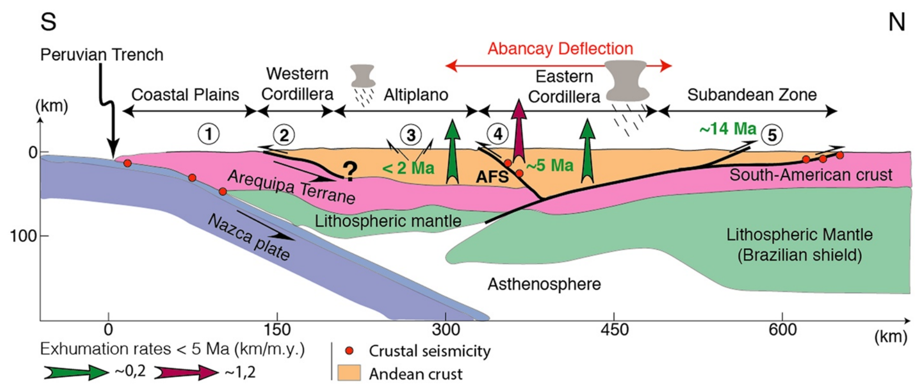

Figure 12. Andean orogenic model (South-North cross section) crossing through the Abancay Deflection since ca. 5 Ma. Modified after the double-verging prism orogenic model of Armijo et al. (2015). Green numbers refer to the initiation timing of the associated crustal deformation. Black circled numbers refer to the compiled previous and present studies: (1) Loewy et al. (2004) and Ramos (2008, 2010); (2) Armijo et al. (2015); (3) Sébrier et al. (1985), Mercier et al. (1992), and Wimpenny et al. (2018); (4) this study; (5) Espurt et al. (2011) and Gautheron et al. (2013). AFS refers to Apurimac fault system.

(Figure 3a) strongly corroborates our interpretation, also supporting the hypothesis that such fault activity and observed exhumation pattern on million-year time scales is still ongoing today.

5.4. Potential Drivers for the Apurimac Fault System Reactivation

The Abancay Deflection is framed northward by the Subandean zone, which has been tectonically active since ca. 14 Ma (Espurt et al., 2011). To the south, the Altiplano is characterized by extensional faulting since the Quaternary (Sébrier et al., 1985; Wimpenny et al., 2018). Our results show that the Eastern Cordillera was tilted through the south-verging backthrust of the Apurimac fault system, which has been active since 8–2 Ma and statistically more likely since ca. 5 Ma (Figures 7b, 9b, 11e, and 12). Considering the orogenic-prism balance theory (Whipple & Meade, 2004; Willett et al., 1993), the tectonic-shortening transfer from the Altiplano to the Subandes (since ca. 15 Ma in Bolivian Andes; Anderson et al., 2018; Horton, 2005; Norton & Schlunegger, 2011) was triggered by sediment accumulation in the foreland basin (i.e., paleo-Subandean zone; Mosolf et al., 2011) following the late Miocene South-American monsoon intensification (Poulsen et al., 2010). Sediment accumulation in the foreland coming from more internal part of the mountain range (which implies mass removal) created a regional stress pattern reorganization that probably triggered eastward propagation of deformation. Thus, the question of the out-of-sequence Apurimac backthrust activity needs to be addressed.

From a morphologic viewpoint, the peculiarity of the Abancay Deflection makes it the only region at the scale of the northern Altiplano where the hydrographic network is reaching the core of the orogen after crossing the entire Eastern Cordillera (Apurimac and Urubamba Rivers; Figures 1 and 11). The river capture, incision, and subsequent increased erosion were probably triggered and enhanced by wetter conditions during the late Miocene (Poulsen et al., 2010) and Pliocene climate variability (Lease & Ehlers, 2013; Peizhen et al., 2001). Given the initiation of reverse faulting at ca. 5 Ma, the Apurimac fault system has played as an out-of-sequence thrust. We thus conceptually interpret in the following the tectonic evolution of the Abancay Deflection (Figures 11 and 12), linking the climate evolution and the tectonic transfer regarding the orogenic-prism rebalancing and geodynamic settings:

(1) Late Miocene precipitation intensification (Poulsen et al., 2010) on the eastern flank of the Peruvian Andesa favored the regressive erosion through the proto-Apurimac and -Urubamba Rivers. These paleodrainage systems captured and incised the internally drained paleo-Abancay Deflection (Figures 11d and 11e).
(2) In consequence to this drainage capture, river incision subsequently enhanced erosional processes over the large-scale Abancay Deflection. Rivers deeply carved the Eastern Cordillera, and sediments were exported toward the foreland basin and trapped within it (in the paleo-Subandes).

Table 4
Compilation of Observations and Comparison of Documented Tectonic Syntaxes With the Abancay Deflection

Observation	Himalayan syntaxis	Alaskan syntaxis	Abancay Deflection
Morphology			
Positive anomaly of topography	YES	YES	YES
	Nanga Parbat mountains (NP); Namche Barwa mountains (NB) (Zeitler et al., 2001)	Denali mountains; St Elias mount (Enkelmann et al., 2017)	Cordillera Vilcabamba (Salcantay, southern Eastern Cordillera) (B. Gérard et al., 2021; B. G. Gérard et al., 2021)
High relief and incision	YES	YES	YES
	Indus River (NP)/Tsangpo River (NB) (Zeitler et al., 2001)	Seward and Logan glaciers (Enkelmann et al., 2017)	Urubamba River (B. Gérard et al., 2021; B. G. Gérard et al., 2021)
Major crossing-orogens rivers	YES	NA[a]	YES
	Indus River (NP)/Tsangpo River (NB) (Zeitler et al., 2001)	Glaciated area	Urubamba River (this study; B. Gérard et al., 2021; B. G. Gérard et al., 2021)
Captured high-elevation plateau upstream	YES	NO	YES
	Tibetan plateau (Clark et al., 2004; Yang et al., 2016)	No plateau	Altiplano (this study; B. Gérard et al., 2021; B. G. Gérard et al., 2021)
Tightened and aligned rivers along active faults	YES	NA[a]	YES
	Salween, Mekong/Yangtze Rivers (NB; Hallet & Molnar, 2001); Hari, Murgab and Helmand Rivers (NP; Brookfield, 1998)	Glaciated area	Urubamba and Apurimac Rivers along the Apurimac fault system (this study; B. Gérard et al., 2021; B. G. Gérard et al., 2021)
Knickpoints	YES	NA[a]	YES
	Tsangpo River crossing the NB (Zeitler et al., 2001)	Masked bedrock beneath the glaciers	Urubamba River crossing the Eastern Cordillera (B. Gérard et al., 2021; B. G. Gérard et al., 2021)
Tectonics and geodynamic			
Tectonic rotation and strike-slip faulting	YES	YES	YES
	Crustal folding through orogen-parallel compression (Royden et al., 1997); Jiali-Parlung fault (NB; Burg et al., 1998); Karakorum fault (NP; Bossart et al., 1988)	Fairweather fault (Chapman et al., 2012)	Counterclockwise rotation and left-lateral component of the Apurimac fault during Miocene (Dalmayrac et al., 1980; Roperch et al., 2006)
Thick-skinned tectonic	YES	YES	YES
	(Zeitler et al., 2001)	(Chapman et al., 2012)	Apurimac fault delimiting two crustal blocks (this study; Carlier et al., 2005)
Localized deformation along crustal-scale faults and magmatic fluid circulation	YES	YES	YES
	(NP; Edwards et al., 2000; Schneider et al., 1999; Seeber & Pêcher, 1998)	Except for fluids circulation (Koons et al., 2010, 2013)	Apurimac fault and volcanic fluids circulation since ~7 Ma (Carlier et al., 1996, 2005)
Indenter	YES	YES	YES
	Indian plate (Burtman & Molnar, 1993)	Yakutat terrane (Koons et al., 2010; Marechal et al., 2015)	Arequipa terrane (Ramos, 2010; Villegas-Lanza et al., 2016)
Higher exhumation rates into the core of the syntaxis	YES	YES	YES
	~10 km/Myr since ~1 Ma (King et al., 2016)	~2 to ~5 km/Myr since ~2 Ma (Enkelmann et al., 2009, 2017; Falkowski et al., 2014)	~1.2 km/Myr since ~5 Ma (this study)
Conclusion			
Tectonic syntaxis	YES	YES	YES

[a]Not applicable.

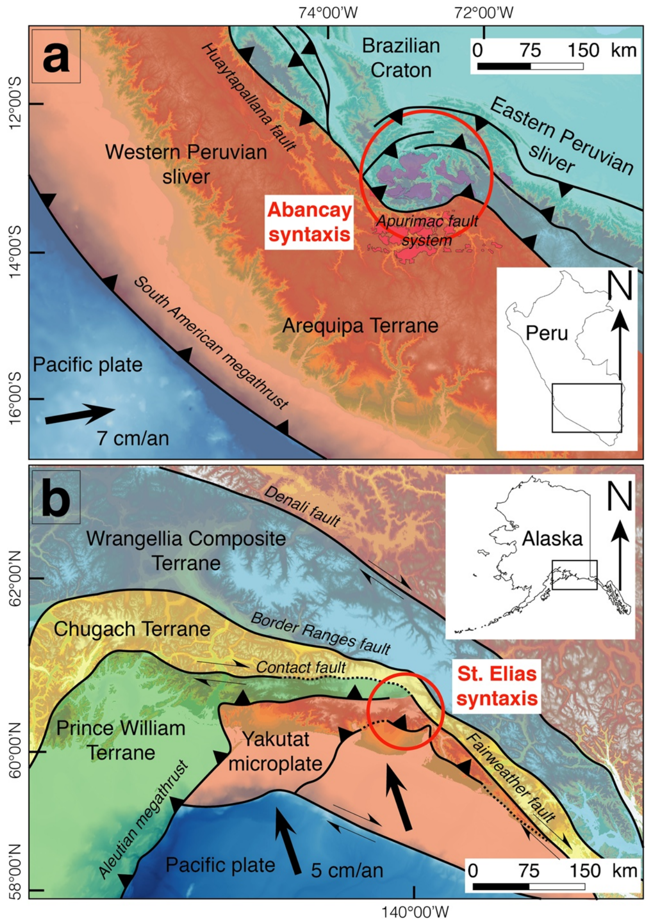

Figure 13. Geodynamic comparison between the Abancay Deflection and the St Elias syntaxis of Alaska. (a) The Abancay Deflection case; the bulls-eye structure and morphology of the Abancay Deflection (red circle) suggest that it is an incipient syntaxis, with the Arequipa terrane acting as the indenter. (b) The St Elias case from Falkowski et al. (2014). The Yakutat microplate plays the role of the indenter for this Alaskan syntaxis.

(3) By orogenic-prism rebalancing, the Subandean deformation propagated northward at ca. 5 Ma (Gautheron et al., 2013; Mosolf et al., 2011). In the core of the orogen, mass removal decreased the taper angle and thus favored tectonically driven rock uplift of the eroding southern Eastern Cordillera through the internal Apurimac fault system (Figures 11e and 12; DeCelles et al., 2009). Concurrently, the generated sediments accumulated in the Subandes have maintained the activity and the propagation of the Subandean front (Gautheron et al., 2013; Mosolf et al., 2011).

(4) Focused deformation localized on the Apurimac fault system may be explained by its specific position and geographic organization, bounding the northern edge of the Arequipa terrane (Figure 12; Loewy et al., 2004). The Arequipa terrane could play the role of a buttress and the deformation could focus on the south-verging lithospheric-scale Apurimac fault system, with the Brazilian shield northward (Figure 12). The northward advance of the Arequipa terrane is still an ongoing process according to GPS measurements that support the current Bolivian Orocline bending (Allmendinger et al., 2005; Villegas-Lanza et al., 2016). In addition, the Apurimac fault system is a lithospheric-scale inherited structure (Carlier et al., 2005; Dalmayrac et al., 1980; Sempere et al., 2002) and constitutes a mechanical weak zone promoting the localization and accumulation of deformation.

Although the Andes present numerous deflected zones (i.e., Cajamarca, Huancabamba in Peru; Dalmayrac et al., 1980), the Abancay Deflection is exceptional with respect to its size, highly rotated fault systems, and its peculiar location at the northern tip of the Altiplano. It marks abruptly the along-strike segmentation of the Central Andes facing the Amazon basin with E-W topographic high. Although backthrusting activity through reactivated Cretaceous crustal normal-fault tilting in the Eastern Cordillera has been already documented in southern Peru (Perez, Horton, & Carlotto, 2016; Perez, Horton, Mcquarrie, et al., 2016), the Apurimac fault system backthrusting is a singularity for this region by its size and inheritance and appears to be one of the main structure articulating the northern narrow Andes versus the southern Bolivian Orocline. This fault system acted as a suture between the eastern Altiplano and the Eastern Cordillera (Jaillard & Soler, 1996) and was reactivated as a backthrust within the last 5 Ma providing stronger uplift in the Eastern Cordillera. The relative position of the Arequipa terrane (Figure 11) acting as a rigid indenter could explain the accumulation of horizontal and vertical deformation in such limited-extend area and the subsequent orthogonal direction of the topography in comparison to the main orogen elongation axis. This could furthermore explain this undocumented tectonic behavior and probable higher erosion rates with an E-W topography facing the Amazonian moisture flux enhancing orographic updraft.

5.5. Is the Abancay Deflection a Tectonic Syntaxis?

According to the geodynamic context with an oblique subduction, as well as the slab dip transition (flat northward vs. steep southward of the Abancay region; Barazangi & Isacks, 1976), the Apurimac fault system could be a contractional duplex developed at bends or a stepover of crustal-scale strike-slip faulting. The Abancay Deflection presents, however, numerous geomorphic, tectonic, and geodynamic features at the origin of the theory of the tectonic syntaxes (Table 4) already documented in the Himalaya (Namche Barwa; Nanga Parbat; e.g., Zeitler et al., 2001) and Alaska (Saint Elias mount; e.g., Enkelmann et al., 2017). Focusing on the Abancay Deflection, high exhumation rates appear concentrated in the core of a distorted zone of limited-extend and framed by deflected active faults, promoting the classification of the Abancay

Deflection as a tectonic syntaxis (this study; Table 4). In this case, the Arequipa terrane could play the role of the indenter in response to counterclockwise rotation (Roperch et al., 2006) of the northern limb of the Bolivian Orocline since the Miocene (Allmendinger et al., 2005; Müller et al., 2002).

The Himalayan syntaxes are characterized by heat advection, subsequent upward deflection of isotherms inducing a brittle–ductile rheological limit to the ascent (Koons et al., 2013). These peculiar thermal and rheological parameters associated with high geothermal gradients (~60°C/km; Craw et al., 1994) and shallow seismicity (~2–5-km depth; Meltzer et al., 1998) are defining tectonic aneurisms (Koons et al., 2013). The Abancay Deflection, however, seems to be relatively "cold" (~20°C/km; this study) and brittle at depth, consistent with geothermal gradient that does not exceed 30°C/km (Eastern Cordillera far south in Bolivia; Barnes et al., 2008; Henry & Pollack, 1988), and crustal seismicity up to 30-km depth, respectively (Figure 3a). Thus, the Abancay Deflection cannot be defined as a tectonic aneurism.

The similarity in structural and geomorphic setting between the Abancay Deflection and the Himalayan/Alaskan syntaxes leads us to speculate that the Abancay Deflection may reflect an incipient Andean syntaxis, where drainage capture and ensuing rapid incision of the plateau edge led to focused exhumation and tectonic uplift along a deflected fault pattern. In such a geodynamic context, associated with ocean–continent convergence, the closest comparison can be done with the Denali syntaxis in Alaska (Figure 13). The Abancay Deflection, however, has not reached yet (and maybe will never do) a mature stage of tectonic aneurism.

6. Conclusions

Our new thermochronological data and inverse thermo(-kinematic) modeling from the Abancay Deflection reveal steady and spatially uniform exhumation for the whole study area between 40 and 5 Ma, at a moderate rate of ~0.2 km/Myr. We interpret such slow and steady exhumation as evidence for large-scale crustal shortening and/or lower crustal flow associated with low-magnitude erosion rates in an internally drained area. The differential exhumation of the Abancay Deflection area initiated at ca. 5 Ma, characterized by around 500% increase in exhumation rate for the southern Eastern Cordillera (~1.2 km/Myr). This 5-Ma exhumation signal has been driven by incision (capture of the paleoendoreic environment) and enhanced by tectonically driven rock uplift along the Apurimac fault system activation as a south-verging backthrust. For the first time, we document the recent (<5 Ma) and ongoing tectonic activity of this fault system. Finally, we propose the late Miocene precipitation intensification and the Arequipa terrane underplating as potential triggers for the reactivation of this out-of-sequence inherited crustal-scale thrust. Considering such a geomorphic and structural setting together with rapid and focused exhumation, in a region of anomalously high relief and topography, we speculate that the Abancay Deflection may represent the first identified incipient Andean syntaxis.

Acknowledgments
This work was supported by the IRD (Institut de Recherche pour le Développement), ISTerre, the INSU (Institut National des Sciences de l'Univers), and the ANR-12-NS06-0005-01 project for the AHe analysis. We are grateful to the SERNANP, the INGEMMET (Cusco-PATA convenio 006-2016-Fondecyt), and the National Archaeological Park of Machu Picchu, for the provided facilities. We thank P. H. Leloup and G. Mahéo (Géode laboratory, Lyon) and the GTC platform (F. Coeur and F. Sénebier, ISTerre, Grenoble) for sample processing, as well as M. Balvay, R. Pinna-Jamme, and F. Haurine for assistance during AFT and AHe dating. We thank Mauricio Parra, Joel Saylor, and an anonymous reviewer for instructive feedbacks on this manuscript.

Data Availability Statement

Data sets for this research are included in this paper (and its supporting information files). Data sets for this research are available at PANGAEA®—Data Publisher for Earth & Environmental Science https://doi.org/10.1594/PANGAEA.929199), [Creative Commons Attribution License].

References

Allmendinger, R. W., Jordan, T. E., Kay, S. M., & Isacks, B. L. (1997). The evolution of the Altiplano-Puna Plateau of the Central Andes. *Annual Review of Earth and Planetary Sciences*, *25*(1), 139–174. https://doi.org/10.1146/annurev.earth.25.1.139

Allmendinger, R. W., Smalley, R., Bevis, M., Caprio, H., & Brooks, B. (2005). Bending the Bolivian Orocline in real time. *Geology*, *33*(11), 905–908. https://doi.org/10.1130/G21779.1

Anderson, R. B., Long, S. P., Horton, B. K., Thomson, S. N., Calle, A. Z., & Stockli, D. F. (2018). Orogenic wedge evolution of the Central Andes, Bolivia (21°S): Implications for Cordilleran cyclicity. *Tectonics*, *37*, 3577–3609. https://doi.org/10.1029/2018TC005132

Armijo, R., Lacassin, R., Coudurier-Curveur, A., & Carrizo, D. (2015). Coupled tectonic evolution of Andean orogeny and global climate. *Earth-Science Reviews*, *143*, 1–35. https://doi.org/10.1016/j.earscirev.2015.01.005

Arndt, J., Bartel, T., Scheuber, E., & Schilling, F. (1997). Thermal and rheological properties of granodioritic rocks from the Central Andes, North Chile. *Tectonophysics*, *271*(1–2), 75–88. https://doi.org/10.1016/S0040-1951(96)00218-1

Ault, A. K., Gautheron, C., & King, G. E. (2019). Innovations in (U–Th)/He, fission track, and trapped charge thermochronometry with applications to earthquakes, weathering, surface–mantle connections, and the growth and decay of mountains. *Tectonics*, *38*, 3705–3739. https://doi.org/10.1029/2018TC005312

Barazangi, M., & Isacks, B. L. (1976). Spatial distribution of earthquakes and subduction of the Nazca plate beneath South America. *Geology*, *4*, 686–692.

Barnes, J. B., & Ehlers, T. A. (2009). End member models for Andean Plateau uplift. *Earth-Science Reviews*, *97*(1–4), 105–132. https://doi.org/10.1016/j.earscirev.2009.08.003

Barnes, J. B., Ehlers, T. A., Insel, N., McQuarrie, N., & Poulsen, C. J. (2012). Linking orography, climate, and exhumation across the Central Andes. *Geology*, *40*(12), 1135–1138. https://doi.org/10.1130/G33229.1

Barnes, J. B., Ehlers, T. A., McQuarrie, N., O'Sullivan, P. B., & Tawackoli, S. (2008). Thermochronometer record of central Andean Plateau growth, Bolivia (19.5°S). *Tectonics*, *27*, TC3003. https://doi.org/10.1029/2007TC002174

Bonhomme, M. G., Fornari, M., Laubacher, G., Sébrier, M., & Vivier, G. (1988). New Cenozoic K–Ar ages on volcanic rocks from the eastern High Andes, southern Peru. *Journal of South American Earth Sciences*, *1*(2), 179–183.

Bossart, P., Dietrich, D., Greco, A., Ottiger, R., & Ramsay, J. G. (1988). The tectonic structure of the Hazara-Kashmir Syntaxis, Southern Himalayas, Pakistan. *Tectonics*, *7*(2), 273–297.

Braun, J. (2003). Pecube: A new finite-element code to solve the 3D heat transport equation including the effects of a time-varying, finite amplitude surface topography. *Computers & Geosciences*, *29*(6), 787–794. https://doi.org/10.1016/S0098-3004(03)00052-9

Braun, J., van der Beek, P., Valla, P., Robert, X., Herman, F., Glotzbach, C., et al. (2012). Quantifying rates of landscape evolution and tectonic processes by thermochronology and numerical modeling of crustal heat transport using PECUBE. *Tectonophysics*, *524–525*(525), 1–28. https://doi.org/10.1016/j.tecto.2011.12.035

Brookfield, M. E. (1998). The evolution of the great river systems of southern Asia during the Cenozoic India-Asia collision: Rivers draining southwards. *Geomorphology*, *22*(3–4), 285–312. https://doi.org/10.1016/S0169-555X(97)00082-2

Brown, R. W., Beucher, R., Roper, S., Persano, C., Stuart, F., & Fitzgerald, P. (2013). Natural age dispersion arising from the analysis of broken crystals. Part I: Theoretical basis and implications for the apatite (U–Th)/He thermochronometer. *Geochimica et Cosmochimica Acta*, *122*(120), 478–497. https://doi.org/10.1016/j.gca.2013.05.041

Burg, J.-P., Nievergelt, P., Oberli, F., Seward, D., Davy, P., Maurin, J.-C., et al. (1998). The Namche Barwa syntaxis: Evidence for exhumation related to compressional crustal folding. *Journal of Asian Earth Sciences*, *16*(2–3), 239–252. https://doi.org/10.1016/S0743-9547(98)00002-6

Burtman, V., & Molnar, P. (1993). Geological and geophysical evidence for deep subduction of continental crust beneath the Pamir. *Geological Society of America Special Paper*, *281*, 1–76.

Butler, R. F., Richards, D. R., Sempere, T., & Marshall, L. G. (1995). Paleomagnetic determinations of vertical-axis tectonic rotations from Late Cretaceous and Paleocene strata of Bolivia. *Geology*, *23*(9), 799–802.

Cabrera, J., Sébrier, M., & Mercier, J. L. (1991). Plio-Quaternary geodynamic evolution of a segment of the Peruvian Andean Cordillera located above the change in the subduction geometry: The Cuzco region. *Tectonophysics*, *190*(2–4), 331–362. https://doi.org/10.1016/0040-1951(91)90437-W

Carlier, G., Lorand, J. P., Bonhomme, M., & Carlotto, V. (1996). A reappraisal of the Cenozoic inner arc magmatism in southern Peru: Consequences for the evolution of the Central Andes for the past 50 Ma. In *Third International Symposium on Andean Geodynamics (ISAG)* (pp. 551–554). Saint Malo, France.

Carlier, G., Lorand, J. P., Liégeois, J. P., Fornari, M., Soler, P., Carlotto, V., & Cárdenas, J. (2005). Potassic-ultrapotassic mafic rocks delineate two lithospheric mantle blocks beneath the southern Peruvian Altiplano. *Geology*, *33*(7), 601–604. Institut de Recherche pour le Développement. https://doi.org/10.1130/G21643.1

Carlotto, V. (2013). Paleogeographic and tectonic controls on the evolution of Cenozoic basins in the Altiplano and Western Cordillera of southern Peru. *Tectonophysics*, *589*, 195–219. https://doi.org/10.1016/j.tecto.2013.01.002

Chapman, J. B., Pavlis, T. L., Bruhn, R. L., Worthington, L. L., Gulick, S. P. S., & Berger, A. L. (2012). Structural relationships in the eastern syntaxis of the St. Elias orogen, Alaska. *Geosphere*, *8*(1), 105–126. https://doi.org/10.1130/GES00677.1

Clark, M. K., Schoenbohm, L. M., Royden, L. H., Whipple, K. X., Burchfiel, B. C., Zhang, X., et al. (2004). Surface uplift, tectonics, and erosion of eastern Tibet from large-scale drainage patterns. *Tectonics*, *23*, TC1006. https://doi.org/10.1029/2002TC001402

Craw, D., Koons, P. O., Winslow, D., Chamberlain, C. P., & Zeitler, P. (1994). Boiling fluids in a region of rapid uplift, Nanga Parbat Massif, Pakistan. *Earth and Planetary Science Letters*, *128*(3–4), 169–182. https://doi.org/10.1016/0012-821X(94)90143-0

Dalmayrac, B., Laubacher, G., & Marocco, R. (1980). *Géologie des Andes péruviennes*. Paris: ORSTOM.

DeCelles, P. G., Ducea, M. N., Kapp, P., & Zandt, G. (2009). Cyclicity in Cordilleran orogenic systems. *Nature Geoscience*, *2*, 251–257. https://doi.org/10.1038/ngeo469

Dorbath, C., Dorbath, L., Cisternas, A., Deverchére, J., & Sebrier, M. (1990). Seismicity of the Huancayo basin (central Peru) and the Huaytapallana fault. *Journal of South American Earth Sciences*, *3*(1), 21–29. https://doi.org/10.1016/0895-9811(90)90015-S

Dziewonski, A. M., Chou, T.-A., & Woodhouse, J. H. (1981). Determination of earthquake source parameters from waveform data for studies of global and regional seismicity. *Journal of Geophysical Research*, *86*(B4), 2825–2852. https://doi.org/10.1029/JB086iB04p02825

Edwards, M. A., Kidd, W. S. F., Khan, M. A., & Schneider, D. A. (2000). Tectonics of the SW margin of the Nanga Parbat-Haramosh massif. *Geological Society, London, Special Publications*, *170*, 77–100.

Egeler, C., & De Booy, T. (1961). Preliminary note on the geology of the Cordillera Vilcabamba (SE Peru), with emphasis on the essentially pre-Andean origin of the structure. *Geologie en Mijnbouw*, *40*(3), 319–325.

Ehlers, T. A., Chaudhri, T., Kumar, S., Fuller, C. W., Willett, S. D., Ketcham, R. A., & Brandon, M. T. (2005). Computational tools for low-temperature thermochronometer interpretation. *Reviews in Mineralogy and Geochemistry*, *58*(1), 589–622. https://doi.org/10.2138/rmg.2005.58.22

Ehlers, T. A., & Poulsen, C. J. (2009). Influence of Andean uplift on climate and paleoaltimetry estimates. *Earth and Planetary Science Letters*, *281*(3–4), 238–248. https://doi.org/10.1016/j.epsl.2009.02.026

Ekström, G., Nettles, M., & Dziewoński, A. M. (2012). The global CMT project 2004–2010: Centroid-moment tensors for 13,017 earthquakes. *Physics of the Earth and Planetary Interiors*, *200–201*, 1–9. https://doi.org/10.1016/j.pepi.2012.04.002

England, P., & Molnar, P. (1990). Surface uplift, uplift of rocks, and exhumation of rocks. *Geology*, *18*, 1173–1177. https://doi.org/10.1130/0091-7613(1990)018<1173:SUUORA>2.3.CO;2

Enkelmann, E., Piestrzeniewicz, A., Falkowski, S., Stübner, K., & Ehlers, T. A. (2017). Thermochronology in southeast Alaska and southwest Yukon: Implications for North American Plate response to terrane accretion. *Earth and Planetary Science Letters*, *457*, 348–358. https://doi.org/10.1016/j.epsl.2016.10.032

Enkelmann, E., Zeitler, P. K., Pavlis, T. L., Garver, J. I., & Ridgway, K. D. (2009). Intense localized rock uplift and erosion in the St Elias orogen of Alaska. *Nature Geoscience*, *2*(5), 360–363. https://doi.org/10.1038/ngeo502

Espurt, N., Barbarand, J., Roddaz, M., Brusset, S., Baby, P., Saillard, M., & Hermoza, W. (2011). A scenario for late Neogene Andean shortening transfer in the Camisea Subandean zone (Peru, 12°S): Implications for growth of the northern Andean Plateau. *The Geological Society of America Bulletin*, *123*(9–10), 2050–2068. https://doi.org/10.1130/B30165.1

Evans, N. J., Byrne, J. P., Keegan, J. T., & Dotter, L. E. (2005). Determination of uranium and thorium in zircon, apatite, and fluorite: Application to laser (U–Th)/He thermochronology. *Journal of Analytical Chemistry*, *60*(12), 1159–1165.

Falkowski, S., Enkelmann, E., & Ehlers, T. A. (2014). Constraining the area of rapid and deep-seated exhumation at the St. Elias syntaxis, Southeast Alaska, with detrital zircon fission-track analysis. *Tectonics*, *33*, 597–616. https://doi.org/10.1002/2013TC003408

Farley, K. A. (2000). Helium diffusion from apatite: General behavior as illustrated by Durango fluorapatite. *Journal of Geophysical Research*, *105*(B2), 2903–2914. https://doi.org/10.1029/1999JB900348

Farley, K. A. (2002). (U–Th)/He dating: Techniques, calibrations, and applications. *Reviews in Mineralogy and Geochemistry*, *47*, 819–844. https://doi.org/10.2138/rmg.2002.47.18

Galbraith, R. F., & Laslett, G. M. (1993). Statistical models for mixed fission track ages. *Nuclear Tracks and Radiation Measurements*, *21*(4), 459–470. https://doi.org/10.1016/1359-0189(93)90185-C

Gallagher, K. (2012). Transdimensional inverse thermal history modeling for quantitative thermochronology. *Journal of Geophysical Research*, *117*, B02408. https://doi.org/10.1029/2011JB008825

Garzione, C. N., McQuarrie, N., Perez, N. D., Ehlers, T. A., Beck, S. L., Kar, N., et al. (2017). Tectonic evolution of the Central Andean plateau and implications for the growth of plateaus. *Annual Review of Earth and Planetary Sciences*, *45*(1), 529–559. https://doi.org/10.1146/annurev-earth-063016-020612

Garzione, C. N., Molnar, P., Libarkin, J. C., & MacFadden, B. J. (2006). Rapid late Miocene rise of the Bolivian Altiplano: Evidence for removal of mantle lithosphere. *Earth and Planetary Science Letters*, *241*(3–4), 543–556. https://doi.org/10.1016/j.epsl.2005.11.026

Gautheron, C., Espurt, N., Barbarand, J., Roddaz, M., Baby, P., Brusset, S., et al. (2013). Direct dating of thick- and thin-skin thrusts in the Peruvian Subandean zone through apatite (U–Th)/He and fission track thermochronometry. *Basin Research*, *25*(4), 419–435. https://doi.org/10.1111/bre.12012

Gautheron, C., & Tassan-Got, L. (2010). A Monte Carlo approach to diffusion applied to noble gas/helium thermochronology. *Chemical Geology*, *273*(3–4), 212–224. https://doi.org/10.1016/j.chemgeo.2010.02.023

Gautheron, C., Tassan-Got, L., Barbarand, J., & Pagel, M. (2009). Effect of alpha-damage annealing on apatite (U–Th)/He thermochronology. *Chemical Geology*, *266*(3–4), 166–179. https://doi.org/10.1016/j.chemgeo.2009.06.001

Gautheron, C., Tassan-Got, L., Ketcham, R. A., & Dobson, K. J. (2012). Accounting for long alpha-particle stopping distances in (U–Th-Sm)/He geochronology: 3D modeling of diffusion, zoning, implantation, and abrasion. *Geochimica et Cosmochimica Acta*, *96*, 44–56. https://doi.org/10.1016/j.gca.2012.08.016

Gérard, B., Audin, L., Robert, X., Gautheron, C., van der Beek, P., Bernet, M., et al. (2021). Pliocene river capture and incision of the northern Altiplano: Machu Picchu, Peru. *Journal of the Geological Society*, *178*(2), 11. https://doi.org/10.1144/jgs2020-100

Gilder, S., Rousse, S., Farber, D., McNulty, B., Sempere, T., Torres, V., & Palacios, O. (2003). Post-Middle Oligocene origin of paleomagnetic rotations in Upper Permian to Lower Jurassic rocks from northern and southern Peru. *Earth and Planetary Science Letters*, *210*(1–2), 233–248. https://doi.org/10.1016/S0012-821X(03)00102-X

Glotzbach, C., van der Beek, P. A., & Spiegel, C. (2011). Episodic exhumation and relief growth in the Mont Blanc massif, Western Alps from numerical modelling of thermochronology data. *Earth and Planetary Science Letters*, *304*(3–4), 417–430. https://doi.org/10.1016/j.epsl.2011.02.020

Gonfiantini, R., Roche, M.-A., Olivry, J.-C., Fontes, J.-C., & Zuppi, G. M. (2001). The altitude effect on the isotopic composition of tropical rains. *Chemical Geology*, *181*, 147–167.

Gotberg, N., McQuarrie, N., & Caillaux, V. C. (2010). Comparison of crustal thickening budget and shortening estimates in southern Peru (12–14°S): Implications for mass balance and rotations in the "Bolivian Orocline". *The Geological Society of America Bulletin*, *122*(5–6), 727–742. https://doi.org/10.1130/B26477.1

Green, P. F. (1981). A new look at statistics in fission-track dating. *Nuclear Tracks*, *5*, 77–86.

Hallet, B., & Molnar, P. (2001). Distorted drainage basins as markers of crustal strain east of the Himalaya. *Journal of Geophysical Research*, *106*(B7), 13697–13709. https://doi.org/10.1029/2000JB900335

Henry, S., & Pollack, H. (1988). Terrestrial heat flow above the Andean subduction zone in Bolivia and Peru. *Journal of Geophysical Research*, *93*(B12), 153–162. https://doi.org/10.1029/JB093iB12p15153

Horton, B. K. (2005). Revised deformation history of the Central Andes: Inferences from Cenozoic foredeep and intermontane basins of the Eastern Cordillera, Bolivia. *Tectonics*, *24*, TC3011. https://doi.org/10.1029/2003TC001619

Horton, B. K., Perez, N. D., Fitch, J. D., & Saylor, J. E. (2014). Punctuated shortening and subsidence in the Altiplano Plateau of southern Peru: Implications for early Andean mountain building. *Lithosphere*, *7*(2), 117–137. https://doi.org/10.1130/L397.1

Husson, L., & Sempere, T. (2003). Thickening the Altiplano crust by gravity-driven crustal channel flow. *Geophysical Research Letters*, *30*(5), 1243. https://doi.org/10.1029/2002GL016877

Insel, N., Poulsen, C. J., & Ehlers, T. A. (2010). Influence of the Andes Mountains on South American moisture transport, convection, and precipitation. *Climate Dynamics*, *35*(7), 1477–1492. https://doi.org/10.1007/s00382-009-0637-1

Jaillard, E., & Soler, P. (1996). Cretaceous to early Paleogene tectonic evolution of the northern Central Andes (0–18°S) and its relations to geodynamics. *Tectonophysics*, *259*(2), 41–53. https://doi.org/10.1016/0040-1951(95)00107-7

James, D. E. (1971). Plate tectonic model for the evolution of the Central Andes. *The Geological Society of America Bulletin*, *82*, 3325–3346. https://doi.org/10.1130/0016-7606(1973)84<1493:PTMFTE>2.0.CO;2

Kar, N., Garzione, C. N., Jaramillo, C., Shanahan, T., Carlotto, V., Pullen, A., et al. (2016). Rapid regional surface uplift of the northern Altiplano plateau revealed by multiproxy paleoclimate reconstruction. *Earth and Planetary Science Letters*, *447*, 33–47. https://doi.org/10.1016/j.epsl.2016.04.025

Kennan, L. (2008). Fission track ages and sedimentary provenance studies in Peru, and their implications for Andean paleogeographic evolution, stratigraphy and hydrocarbon systems. In *VI INGEPET, 13–17 October 2008* (p. 13). Lima, Peru: INGEPET. Retrieved from http://www.agu.org/pubs/crossref/1988/JB093iB12p15153.shtml

Ketcham, R. A., Carter, A., Donelick, R. A., Barbarand, J., & Hurford, A. J. (2007). Improved modeling of fission-track annealing in apatite. *American Mineralogist*, *92*(5–6), 799–810. https://doi.org/10.2138/am.2007.2281

Ketcham, R. A., Donelick, R. A., & Carlson, W. D. (1999). Variability of apatite fission-track annealing kinetics: III. Extrapolation to geological time scales. *American Mineralogist*, *84*, 1235–1255. https://doi.org/10.2138/am-1999-0902

Ketcham, R. A., Gautheron, C., & Tassan-Got, L. (2011). Accounting for long alpha-particle stopping distances in (U–Th–Sm)/He geochronology: Refinement of the baseline case. *Geochimica et Cosmochimica Acta*, *75*(24), 7779–7791. https://doi.org/10.1016/j.gca.2011.10.011

King, G. E., Herman, F., & Guralnik, B. (2016). Northward migration of the eastern Himalayan syntaxis revealed by OSL thermochronometry. *Science*, *353*(6301), 800–804. https://doi.org/10.1126/science.aaf2637

Koons, P. O., Hooks, B. P., Pavlis, T., Upton, P., & Barker, A. D. (2010). Three-dimensional mechanics of Yakutat convergence in the southern Alaskan plate corner. *Tectonics*, *29*, TC4008. https://doi.org/10.1029/2009TC002463

Koons, P. O., Zeitler, P. K., & Hallet, B. (2013). Tectonic aneurysms and mountain building. In Treatise on geomorphology (Vol. 5, pp. 318–349). Elsevier Inc. https://doi.org/10.1016/B978-0-12-374739-6.00094-4

Lamb, S. (2011). Did shortening in thick crust cause rapid Late Cenozoic uplift in the northern Bolivian Andes? *Journal of the Geological Society*, *168*(5), 1079–1092. https://doi.org/10.1144/0016-76492011-008

Lancelot, J. R., Laubacher, G., Marocco, R., & Renaud, U. (1978). U/Pb radiochronology of two granitic plutons from the Eastern Cordillera (Peru)—Extent of Permian magmatic activity and consequences. *Geologische Rundschau*, *67*(1), 236–243. https://doi.org/10.1007/BF01803263

Lease, R. O., & Ehlers, T. A. (2013). Incision into the eastern Andean Plateau during Pliocene cooling. *Science*, *341*(6147), 774–776. https://doi.org/10.1126/science.1239132

Loewy, S. L., Connelly, J. N., & Dalziel, I. W. D. (2004). An orphaned basement block: The Arequipa-Antofalla Basement of the central Andean margin of South America. *The Geological Society of America Bulletin*, *116*(1–2), 171–187. https://doi.org/10.1130/B25226.1

Mamani, M., Wörner, G., & Sempere, T. (2010). Geochemical variations in igneous rocks of the Central Andean orocline (13°S to 18°S): Tracing crustal thickening and magma generation through time and space. *The Geological Society of America Bulletin*, *122*(1–2), 162–182. https://doi.org/10.1130/B26538.1

Marechal, A., Mazzotti, S., Elliott, J. L., Freymueller, J. T., & Schmidt, M. (2015). Indentor-corner tectonics in the Yakutat-St. Elias collision constrained by GPS. *Journal of Geophysical Research: Solid Earth*, *120*, 3897–3908. https://doi.org/10.1002/2015JB012608

Marocco, R. (1971). Etude géologique de la chaîne andine au niveau de la déflexion d'Abancay (Pérou). *Cahiers ORSTOM Série Géologie*, *3*, 45–58.

Meltzer, A. S., Sarker, G. L., Seeber, L., & Armbruster, J. (1998). Snap, crackel, pop! Seismicity and crustal structure at Nanga Parbat, Pakistan, Himalaya. *Eos Transactions, American Geophysical Union*, *79*, F909.

Mercier, L., Sébrier, M., Lavenu, A., Cabrera, J., Bellier, O., Dumont, J. ., & Machare, J. (1992). Changes in the tectonic regime above a subduction zone of Andean type: The Andes of Peru and Bolivia during the Pliocene–Pleistocene. *Journal of Geophysical Research*, *97*(B8), 945–982.

Mišković, A., Spikings, R. A., Chew, D. M., Košler, J., Ulianov, A., & Schaltegger, U. (2009). Tectonomagmatic evolution of Western Amazonia: Geochemical characterization and zircon U–Pb geochronologic constraints from the Peruvian Eastern Cordilleran granitoids. *Bulletin of the Geological Society of America*, *121*(9–10), 1298–1324. https://doi.org/10.1130/B26488.1

Mosolf, J. G., Horton, B. K., Heizler, M. T., & Matos, R. (2011). Unroofing the core of the central Andean fold-thrust belt during focused late Miocene exhumation: Evidence from the Tipuani-Mapiri wedge-top basin, Bolivia. *Basin Research*, *23*(3), 346–360. https://doi.org/10.1111/j.1365-2117.2010.00491.x

Müller, J. P., Kley, J., & Jacobshagen, V. (2002). Structure and Cenozoic kinematics of the Eastern Cordillera, southern Bolivia (21°S). *Tectonics*, *21*(5), 1037. https://doi.org/10.1029/2001TC001340

Norton, K., & Schlunegger, F. (2011). Migrating deformation in the Central Andes from enhanced orographic rainfall. *Nature Communications*, *2:584*(1). 7. https://doi.org/10.1038/ncomms1590

Ouimet, W. B., & Cook, K. L. (2010). Building the Central Andes through axial lower crustal flow. *Tectonics*, *29*, TC3010. https://doi.org/10.1029/2009TC002460

Peizhen, Z., Molnar, P., & Downs, W. R. (2001). Increased sedimentation rates and grain sizes 2–4 Ma ago due to the influence of climate change on erosion rates. *Nature*, *410*, 891–897.

Perello, J., Carlotto, V., Zarate, A., Ramos, P., Posso, H., Neyra, C., et al. (2003). Porphyry-style alteration and mineralization of the Middle Eocene to Early Oligocene Andahuaylas-Yauri Belt, Cuzco Region, Peru. *Economic Geology*, *98*, 1575–1605.

Perez, N. D., Horton, B. K., & Carlotto, V. (2016). Structural inheritance and selective reactivation in the Central Andes: Cenozoic deformation guided by pre-Andean structures in southern Peru. *Tectonophysics*, *671*, 264–280. https://doi.org/10.1016/j.tecto.2015.12.031

Perez, N. D., Horton, B. K., Mcquarrie, N., Stübner, K., & Ehlers, T. A. (2016). Andean shortening, inversion and exhumation associated with thin- and thick-skinned deformation in southern Peru. *Geological Magazine*, *153*, 1013–1041. https://doi.org/10.1017/S0016756816000121

Phillips, K., Clayton, R. W., Davis, P., Tavera, H., Guy, R., Skinner, S., et al. (2012). Structure of the subduction system in southern Peru from seismic array data. *Journal of Geophysical Research*, *117*, B11306. https://doi.org/10.1029/2012JB009540

Poulsen, C. J., Ehlers, T. A., & Insel, N. (2010). Onset of convective rainfall during gradual late Miocene rise of the Central Andes. *Science*, *328*, 490–494. https://doi.org/10.1126/science.1185078

Rak, A. J., McQuarrie, N., & Ehlers, T. A. (2017). Kinematics, exhumation, and sedimentation of the North Central Andes (Bolivia): An integrated thermochronometer and thermokinematic modeling approach. *Tectonics*, *36*, 2524–2554. https://doi.org/10.1002/2016TC004440

Ramos, V. A. (2008). The basement of the Central Andes: The Arequipa and related terranes. *Annual Review of Earth and Planetary Sciences*, *36*(1), 289–324. https://doi.org/10.1146/annurev.earth.36.031207.124304

Ramos, V. A. (2010). The Grenville-age basement of the Andes. *Journal of South American Earth Sciences*, *29*(1), 77–91. https://doi.org/10.1016/j.jsames.2009.09.004

Recanati, A., Gautheron, C., Barbarand, J., Missenard, Y., Pinna-Jamme, R., Tassan-Got, L., et al. (2017). Helium trapping in apatite damage: Insights from (U–Th–Sm)/He dating of different granitoid lithologies. *Chemical Geology*, *470*, 116–131. https://doi.org/10.1016/j.chemgeo.2017.09.002

Reiners, P. W., & Brandon, M. T. (2006). Using thermochronology to understand orogenic erosion. *Annual Review of Earth and Planetary Sciences*, *34*(1), 419–466. https://doi.org/10.1146/annurev.earth.34.031405.125202

Reiners, P. W., & Shuster, D. L. (2009). Thermochronology and landscape evolution. *Physics Today*, *62*, 31–36.

Reitsma, M. J. (2012). *Reconstructing the Late Paleozoic–Early Mesozoic plutonic and sedimentary record of south-east Peru: Orphaned backarcs along the western margin of Gondwana*. Université de Genève.

Richards, D. R., Butler, R. F., & Sempere, T. (2004). Vertical-axis rotations determined from paleomagnetism of Mesozoic and Cenozoic strata of the Bolivian Andes. *Journal of Geophysical Research*, *109*, B07104. https://doi.org/10.1029/2004JB002977

Robert, X., Van Der Beek, P., Braun, J., Perry, C., & Mugnier, J. L. (2011). Control of detachment geometry on lateral variations in exhumation rates in the Himalaya: Insights from low-temperature thermochronology and numerical modeling. *Journal of Geophysical Research*, *116*, B05202. https://doi.org/10.1029/2010JB007893

Roperch, P., Carlotto, V., Ruffet, G., & Fornari, M. (2011). Tectonic rotations and transcurrent deformation south of the Abancay Deflection in the Andes of southern Peru. *Tectonics*, *30*, TC2010. https://doi.org/10.1029/2010TC002725

Roperch, P., Sempere, T., Macedo, O., Arriagada, C., Fornari, M., Tapia, C., et al. (2006). Counterclockwise rotation of late Eocene–Oligocene fore-arc deposits in southern Peru and its significance for oroclinal bending in the Central Andes. *Tectonics*, *25*, TC3010. https://doi.org/10.1029/2005TC001882

Rousse, S., Gilder, S., Fornari, M., & Sempere, T. (2005). Insight into the Neogene tectonic history of the northern Bolivian Orocline from new paleomagnetic and geochronologic data. *Tectonics*, *24*, TC6007. https://doi.org/10.1029/2004TC001760

Royden, L. H., Burchfiel, B. C., King, R. W., Wang, E., Chen, Z., Shen, F., & Liu, Y. (1997). Surface deformation and lower crustal flow in eastern Tibet. *Science*, *276*(5313), 788–790. https://doi.org/10.1126/science.276.5313.788

Ruiz, G. M. H., Carlotto, V., Van Heiningen, P. V., & Andriessen, P. A. M. (2009). Steady-state exhumation pattern in the Central Andes—SE Peru. *Geological Society, London, Special Publications*, *324*(1), 307–316. https://doi.org/10.1144/SP324.20

Sambridge, M. (1999a). Geophysical inversion with a neighborhood algorithm—I. Searching a parameter space. *Geophysical Journal International*, *138*(2), 479–494. https://doi.org/10.1046/j.1365-246X.1999.00876.x

Sambridge, M. (1999b). Geophysical inversion with a neighborhood algorithm—II. Appraising the ensemble. *Geophysical Journal International*, *138*, 727–746.

Schneider, D. A., Edwards, M. A., Kidd, W. S. F., Asif Khan, M., Seeber, L., & Zeitler, P. K. (1999). Tectonics of Nanga Parbat, western Himalaya: Synkinematic plutonism within the doubly vergent shear zones of a crustal-scale pop-up structure. *Geology*, *27*(11), 999–1002. https://doi.org/10.1130/0091-7613(1999)027<0999:TONPWH>2.3.CO;2

Schwarz, G. E. (1978). Estimating the dimension of a model. *The Annals of Statistics*, *6*, 461–464.

Sébrier, M., Mercier, J. L., Mégard, F., Laubacher, G., & Carey-Gailhardis, E. (1985). Quaternary normal and reverse faulting and the state of stress in the Central Andes of South Peru. *Tectonics*, *4*(7), 739–780.

Seeber, L., & Pêcher, A. (1998). Strain partitioning along the Himalayan arc and the Nanga Parbat antiform. *Geology*, *26*(9), 791–794. https://doi.org/10.1130/0091-7613(1998)026<0791:SPATHA>2.3.CO;2

Sempere, T., Carlier, G., Soler, P., Fornari, M., Carlotto, V., Jacay, J., et al. (2002). Late Permian–Middle Jurassic lithospheric thinning in Peru and Bolivia, and its bearing on Andean-age tectonics. *Tectonophysics*, *345*(1–4), 153–181. https://doi.org/10.1016/S0040-1951(01)00211-6

Shuster, D. L., Flowers, R. M., & Farley, K. A. (2006). The influence of natural radiation damage on helium diffusion kinetics in apatite. *Earth and Planetary Science Letters*, *249*(3–4), 148–161. https://doi.org/10.1016/j.epsl.2006.07.028

Sobolev, S. V., & Babeyko, A. Y. (2005). What drives orogeny in the Andes? *Geology*, *33*(8), 617–620. https://doi.org/10.1130/G21557.1

Springer, M. (1999). Interpretation of heat-flow density in the Central Andes. *Tectonophysics*, *306*, 377–395. https://doi.org/10.1016/S0040-1951(99)00067-0

Stüwe, K., White, L., & Brown, R. (1994). The influence of eroding topography on steady-state isotherms. Application to fission track analysis. *Earth and Planetary Science Letters*, *124*, 63–74.

Strecker, M. R., Alonso, R. N., Bookhagen, B., Carrapa, B., Hilley, G. E., Sobel, E. R., & Trauth, M. H. (2007). Tectonics and climate of the Southern Central Andes. *Annual Review of Earth and Planetary Sciences*, *35*(1), 747–787. https://doi.org/10.1146/annurev.earth.35.031306.140158

Suárez, G., Molnar, P., & Burchfiel, B. C. (1983). Seismicity, fault plane solutions, depth of faulting, and active tectonics of the Andes of Peru, Ecuador, and southern Colombia. *Journal of Geophysical Research*, *88*(B12), 10403–10428. https://doi.org/10.1029/JB088iB12p10403

Sundell, K. E., Saylor, J. E., Lapen, T. J., & Horton, B. K. (2019). Implications of variable late Cenozoic surface uplift across the Peruvian Central Andes. *Scientific Reports*, *9*(1), 1–12. https://doi.org/10.1038/s41598-019-41257-3

Tassara, A. (2005). Interaction between the Nazca and South American plates and formation of the Altiplano-Puna plateau: Review of a flexural analysis along the Andean margin (15°–34°S). *Tectonophysics*, *399*(1–4 SPEC. ISS.), 39–57. https://doi.org/10.1016/j.tecto.2004.12.014

Valla, P. G., Van Der Beek, P. A., Shuster, D. L., Braun, J., Herman, F., Tassan-Got, L., & Gautheron, C. (2012). Late Neogene exhumation and relief development of the Aar and Aiguilles Rouges massifs (Swiss Alps) from low-temperature thermochronology modeling and ^{4}He/^{3}He thermochronometry. *Journal of Geophysical Research*, *117*, F01004. https://doi.org/10.1029/2011JF002043

Villegas-Lanza, J. C., Chlieh, M., Cavalié, O., Tavera, H., Baby, P., Chire-Chira, J., & Nocquet, J.-M. (2016). Active tectonics of Peru: Heterogeneous interseismic coupling along the Nazca megathrust, rigid motion of the Peruvian Sliver, and Subandean shortening accommodation. *Journal of Geophysical Research: Solid Earth*, *121*, 7371–7394. https://doi.org/10.1002/2015JB012608

Whipple, K. X., & Meade, B. J. (2004). Controls on the strength of coupling among climate, erosion, and deformation in two-sided, frictional orogenic wedges at steady state. *Journal of Geophysical Research*, *109*, F01011. https://doi.org/10.1029/2003JF000019

Whittington, A. G., Hofmeister, A. M., & Nabelek, P. I. (2009). Temperature-dependent thermal diffusivity of the Earth's crust and implications for magmatism. *Nature*, *458*(7236), 319–321. https://doi.org/10.1038/nature07818

Willett, S., Beaumont, C., & Fullsack, P. (1993). Mechanical model for the tectonics of doubly vergent compressional orogens. *Geology*, *21*(4), 371–374. https://doi.org/10.1130/0091-7613(1993)021<0371:MMFTTO>2.3.CO;2

Wimpenny, S., Benavente, C., Copley, A., Garcia, B., Rosell, L., O'Kane, A., & Aguirre, E. (2020). Observations and dynamical implications of active normal faulting in South Peru. *Geophysical Journal International*, *222*(1), 27–53. https://doi.org/10.1093/gji/ggaa144

Wimpenny, S., Copley, A., Benavente, C., & Aguirre, E. (2018). Extension and dynamics of the Andes inferred from the 2016 Parina (Huarichancara) earthquake. *Journal of Geophysical Research: Solid Earth*, *123*, 8198–8228. https://doi.org/10.1029/2018JB015588

Yang, R., Fellin, M. G., Herman, F., Willett, S. D., Wang, W., & Maden, C. (2016). Spatial and temporal pattern of erosion in the Three Rivers Region, southeastern Tibet. *Earth and Planetary Science Letters*, *433*, 10–20. https://doi.org/10.1016/j.epsl.2015.10.032

Zeitler, P. K., Meltzer, A. S., Koons, P. O., Craw, D., Hallet, B., Chamberlain, C. P., et al. (2001). Erosion, Himalayan geodynamics, and the geomorphology of metamorphism. *Geological Society of America Today*, *11*, 4–9.